



저작자표시-비영리-동일조건변경허락 2.0 대한민국

이용자는 아래의 조건을 따르는 경우에 한하여 자유롭게

- 이 저작물을 복제, 배포, 전송, 전시, 공연 및 방송할 수 있습니다.
- 이차적 저작물을 작성할 수 있습니다.

다음과 같은 조건을 따라야 합니다:



저작자표시. 귀하는 원저작자를 표시하여야 합니다.



비영리. 귀하는 이 저작물을 영리 목적으로 이용할 수 없습니다.



동일조건변경허락. 귀하가 이 저작물을 개작, 변형 또는 가공했을 경우에는, 이 저작물과 동일한 이용허락조건하에서만 배포할 수 있습니다.

- 귀하는, 이 저작물의 재이용이나 배포의 경우, 이 저작물에 적용된 이용허락조건을 명확하게 나타내어야 합니다.
- 저작권자로부터 별도의 허가를 받으면 이러한 조건들은 적용되지 않습니다.

저작권법에 따른 이용자의 권리는 위의 내용에 의하여 영향을 받지 않습니다.

이것은 [이용허락규약\(Legal Code\)](#)을 이해하기 쉽게 요약한 것입니다.

[Disclaimer](#)



저작자표시-비영리-동일조건변경허락 2.0 대한민국

이용자는 아래의 조건을 따르는 경우에 한하여 자유롭게

- 이 저작물을 복제, 배포, 전송, 전시, 공연 및 방송할 수 있습니다.
- 이차적 저작물을 작성할 수 있습니다.

다음과 같은 조건을 따라야 합니다:



저작자표시. 귀하는 원저작자를 표시하여야 합니다.



비영리. 귀하는 이 저작물을 영리 목적으로 이용할 수 없습니다.



동일조건변경허락. 귀하가 이 저작물을 개작, 변형 또는 가공했을 경우에는, 이 저작물과 동일한 이용허락조건하에서만 배포할 수 있습니다.

- 귀하는, 이 저작물의 재이용이나 배포의 경우, 이 저작물에 적용된 이용허락조건을 명확하게 나타내어야 합니다.
- 저작권자로부터 별도의 허가를 받으면 이러한 조건들은 적용되지 않습니다.

저작권법에 따른 이용자의 권리는 위의 내용에 의하여 영향을 받지 않습니다.

이것은 [이용허락규약\(Legal Code\)](#)을 이해하기 쉽게 요약한 것입니다.

[Disclaimer](#)

이학석사 학위논문

백금 기반의 속빈 나노 셸 구조물의 제조와 특성 연구

**Fabrication, Catalysis, and Surface-Plasmon Resonances
of Hollow Platinum Nanobubbles**

2013 년 8 월

서울대학교 대학원
화학부 물리화학 전공
곽진아

**Fabrication, Catalysis, and Surface-Plasmon Resonances
of Hollow Platinum Nanobubbles**

by Jin-Ah Kwak

Supervisor: Professor Du-Jeon Jang

Major: Physical Chemistry

School of Chemistry
Graduate School of
Seoul National University

August 2013

백금 기반의 속빈 나노 셸 구조물의 제조와 특성 연구

**Fabrication, Catalysis, and Surface-Plasmon Resonances
of Hollow Platinum Nanobubbles**

지도교수 장 두 전

이 논문을 이학석사 학위논문으로 제출함

2013년 8월

서울대학교 대학원

화학부 물리화학 전공

곽진아

곽진아의 석사학위논문을 인준함

2013년 8월

위 원 장 강 현 (서명)

부 위 원 장 장 두 전 (서명)

위 원 홍 병 희 (서명)

Abstract of Dissertation

The catalytic and optical properties of platinum-based nanostructures have been investigated using the time-dependent and static UV-Vis absorption spectra, and the extended Mie theory calculation.

Chapter 1 describes the catalytic properties of the platinum nanobubbles via the degradation reaction of rhodamine B in the presence of potassium borohydride. We have accounted for the catalysis mechanisms using the kinetic parameters (rate constant, activation energies, frequency factors, entropies of activation, and enthalpies of activation) obtained from the first order kinetics, Arrhenius and Eyring equations.

Chapter 2 presents the surface plasmon resonance of platinum nanobubbles having 148 nm diameter and 11 nm shell thickness. Platinum nanoshells with silica cores or hollow interiors have been dispersed in water, ethanol, and dibutyl ether to examine the solvent effects on the optical extinction spectra and compared with the calculated spectra obtained from the extended Mie theory calculation.

Chapter 3 describes the laser-induced nanowelding process of platinum nanobubbles using the nanosecond laser. Platinum nanobubbles have been connected linearly and become thick based on size reduction by the thermalized photon energy of surface-plasmon excitation. Their catalytic properties also

have been investigated based on the effect of shape transformation.

Keywords: Platinum, Nanobubbles, Core-shell nanospheres, Catalysis, Surface plasmon resonance, Mie theory, Laser welding process

Student Number: 2011-23214

Contents

Abstract of Dissertation	i
List of Figures and Tables	1
Chapter 1. Facile Fabrication of Platinum Nanobubbles Having Efficient Catalytic Degradation Performances	5
1.1. Abstract	6
1.2. Introduction	7
1.3. Experimental Section	11
1.4. Results and Discussion	14
1.5. Conclusions	25
1.6. Acknowledgement	27
1.7. Supporting Information	28
1.8. References	29
Chapter 2. Facile Fabrication of Platinum Nanobubbles Having Efficient Catalytic Degradation Performances	33
2.1. Abstract	34
2.2. Introduction	35
2.3. Experimental Section	38

2.4. Results and Discussion	40
2.5. Conclusions	48
2.6. References	49
Chapter 3. Enhanced Catalytic Performances of Linear-Connected Platinum Nanobubbles via Laser Welding Process	51
3.1. Abstract	52
3.2. Introduction	53
3.3. Experimental Section	56
3.4. Results and Discussion	58
3.5. Conclusions	66
3.6. References	67
Appendices	
A.1. List of Publications	70
A.2. List of Presentations	71
Abstract (Korean)	72

List of Figures and Tables

Figure 1-1. Schematic for the fabrication of platinum nanobubbles.

Figure 1-2. Transmission electron microscopy (TEM) images of platinum nanobubbles with average diameters of 150 (top), 320 (middle), and 420 nm (bottom).

Figure 1-3. Area-normalized EDX elemental profiles of a platinum nanobubble scanned along the line in the HRTEM image of the inset. Squares indicate Pt while circles and crosses do Si and O, respectively.

Figure 1-4. Absorption spectra at 30 °C of 10 μ M rhodamine B solutions in the presence of 1.2 mM KBH_4 after addition of (a) SiO_2 @Pt core-shell nanospheres having an average diameter of 150 nm (150C) and (b) platinum nanobubbles having average outer diameters of 150 nm (150H), (c) 320 nm (320H), and (d) 420 nm (420H), measured at elapsed times indicated in the units of min.

Figure 1-5. First-order kinetics, $\ln(A/A_0)$ vs t , for the catalytic degradation of 10 μ M rhodamine B via nanocatalysts of (a) 150C and (b) 150H in the presence of 1.2 mM KBH_4 at temperatures indicated in the units of Celsius degrees.

Figure 1-6. (a) Arrhenius plots for the catalytic degradation reaction of 10

μM rhodamine B in the presence of 1.2 mM KBH_4 via platinum nanocatalysts indicated inside. (b) The compensation law plot of the activation energies and the frequency factors obtained from the slopes and the intercepts, respectively, of the Arrhenius plots.

Table 1-1. Comparison of rate constants, frequency factors, activation energies, and activation entropies for the catalytic degradation of rhodamine B via platinum nanocatalysts in the presence of KBH_4 .

Figure 2-1. Transmission electron microscopy (TEM) images of (a) $\text{SiO}_2@Pt$ core-shell nanospheres and (b) Pt nanobubbles. Scanning electron microscopy (SEM) images of (c) $\text{SiO}_2@Pt$ core-shell nanospheres and (d) Pt nanobubbles, respectively.

Figure 2-2. Representative experimental extinction spectra of (a) $\text{SiO}_2@Pt$ core-shell nanospheres and (b) Pt nanobubbles dispersed in H_2O (red), EtOH (blue), and dibutyl ether (green).

Figure 2-3. Geometry of the nanoshell structures: ϵ_n ($n = 1, 2, 3$) is the dielectric constant of the core, shell, and surrounding medium. r_1 and r_2 are radius of core and core-shell nanospheres, respectively.

Figure 2-4. Extended Mie theory calculations (red) and experimental data (black) of the absorption efficiency spectra. (a,c,e) $\text{SiO}_2@Pt$ core-shell nanospheres and (b,e,f) Pt nanobubbles having a uniform thickness of 20 nm with average outer diameters of 148 nm were dispersed in water (top), ethanol (middle), and dibutyl ether (bottom), respectively.

Figure 2-5. Mie theory calculations (solid line) of absorption (blue), scattering (red), and extinction (black) and experimental data (dotted line). (a) SiO₂@Pt core-shell nanospheres and (b) Pt nanobubbles are dispersed in water, respectively.

Table 2-1. Dielectric constants of each regions of nanostructures. The number in the bracket is numerical value used for the calculation.

Figure 3-1. Schematic description for the laser-induced fabrication of the connected platinum nanobubbles.

Figure 3-2. Transmission electron microscopy (TEM) images of (a) platinum nanobubbles and (b) laser-induced platinum nanobubbles connected in a line via the laser welding process.

Figure 3-3. (a) EDX elemental line scanning and (b) mapping profiles of laser-induced platinum nanobubbles in the HRTEM image of the inset.

Figure 3-4. Absorption spectra at 30 °C of 11 μM rhodamine B solutions in the presence of 1.3 mM KBH₄ after addition of (a) SiO₂@Pt core-shell nanospheres (CNSs), (b) platinum nanobubbles (HNBs), (c) laser-induced SiO₂@Pt core-shell nanospheres (L-CNSs), and (d) laser-induced platinum nanobubbles (L-HNBs).

Figure 3-5. The linear relationship between $\ln (A/A_0)$ of rhodamine B corresponding to the rhodamine B degradation by potassium borohydride and

the time of the reaction in minutes via the nanocatalysts of (a) L-HNBs and (b) L-CNSs.

Figure 3-6. The Arrhenius plots for the catalytic degradation reaction of 11 μM rhodamine B solutions in the presence of 1.3 mM KBH_4 via platinum nanocatalysts indicated inside.

Table 3-1. Comparison of the observed rate constants of the catalytic degradation of rhodamine B in the presence of potassium borohydride at different temperatures when catalyzed by L-HNBs and L-CNSs.

Chapter 1. Facile Fabrication of Platinum Nanobubbles Having Efficient Catalytic Degradation Performances[†]

[†] This chapter is reproduced from Jin-Ah Kwak, Dong Ki Lee, and Du-Jeon Jang, *Appl. Catal.*

B: Environ., **2013**, 142-143, 323-328. © 2013 Elsevier B.V.

1.1. Abstract

Platinum nanobubbles having a uniform shell thickness of 20 nm with average outer diameters of 150, 320, and 420 nm have been synthesized readily by etching the silica cores of SiO₂@Pt core-shell nanospheres and they have been found to catalyze the degradation of rhodamine B efficiently in the presence of KBH₄ compared with SiO₂@Pt core-shell nanospheres. The catalytic rate constant of the nanobubbles (0.030 min⁻¹) with an activation energy of 10.7 kcal mol⁻¹ is larger by 23 times than that of the core-shell nanospheres with an activation energy of 30.5 kcal mol⁻¹. The catalytic activation energy and the entropy of activation obtained from the Arrhenius and the Eyring plots, respectively, have been found to increase with the size increase of platinum nanobubbles, due to the reduction of the nanoreactor confinement effect of platinum nanobubbles. The existence of a good compensation effect between activation energies and frequency factors has been evidenced to support that the catalytic degradation reaction takes place within the nanocavities of platinum nanocatalysts.

1.2. Introduction

The controlled fabrication, characterization, and application of nanometer-sized materials with functional properties have been studied widely [1-5]. In particular, noble-metal nanostructures with different sizes and shapes have been studied extensively, because they can be possibly used in diverse applications such as catalysts, devices, transistors, and optoelectronics [6,7]. Various properties of noble-metal nanostructures, which are very different from those of bulk materials, can be changed by controlling sizes and shapes, because their unusual properties arise from their large surface area-to-volume ratio and the spatial confinement of electrons, phonons, and electric fields in and around them [8]. Noble-metal nanoparticles show strong UV/vis absorption bands depending on sizes and shapes due to the collective excitations of electrons in the conduction band, known as localized surface plasmon resonances [9-13]. Among various noble-metal nanostructures, platinum-based nanostructures especially have attracted widespread interest as platinum plays an outstanding role in multifunctional catalysts for many industrial reactions [14,15]. However, because there are some crucial obstacles such as low platinum-utilization efficiency and high cost, some ways must be found to reduce the amount of platinum used in specific applications by increasing its catalytic activity in order to lower the overall cost [16]. Thus, it is necessary to thoroughly understand the

behaviours of platinum nanoparticles in nanocatalysis. The waste water produced in textile and dye industry has a very bad effect on the environment, due to their large discharge volume and toxic composition. With the development of dye industry, the studies on the treatment of waste water containing dyestuffs have become increasingly important [17]. The decomposition of these organic pollutants via catalytic oxidation or reduction using nanocatalysts is considered to be the most efficient green method for the management of organic wastes [18]. Treatment with strong reducing agents such as KBH_4 can reduce color in dye effluents such as rhodamine B. The reducing compounds chemically break the double bonds of azo dyes and produce aromatic amines of lower molecular weight [19].

Various strategies have been developed to improve the performance of platinum catalysts. In particular, the reactivity of platinum nanocatalysts depends highly on their structures, so many researchers have studied the morphology of platinum nanostructures and have synthesized diverse nanostructures of platinum. For example, El-Sayed et al. have compared the stability and catalytic activities of tetrahedral, spherical, and cubic platinum nanoparticles with different sizes for the electron-transfer reaction between hexacyanoferrate ions and thiosulfate ions. The catalytic activity of nearly spherical nanoparticles has been reported to be intermediate between those of tetrahedral and cubic nanoparticles [20,21]. Considerable studies have been

focused on the syntheses of variously shape-controlled platinum nanostructures such as nanospheres, nanorods, nanowires, nanotubes, and nanodendrites [22-26]. Especially, hollow-structured platinum nanoparticles can be applied to nanometer-sized chemical reactors, efficient catalysts, and energy-storage media, and small containers to encapsulate multi-functional active materials, and they have structurally tunable features such as thickness, interior cavity size, and chemical composition [27,28]. In general, the syntheses of hollow nanostructures have been based on specific theories like the Kirkendall effect, the Ostward ripening, and the layer-by-layer assembly, and they can be divided into four categories: conventional hard-templating, sacrificial-templating, soft-templating, and template-free methods [29-32].

Herein, we demonstrate a facile and efficient method to synthesize platinum-based nanocatalysts having nanobubble structures using a conventional hard template (Fig. 1). The preparation of hollow structures by using against a hard material as templates is conceptually straightforward, and it involves four major steps: the preparation of hard templates, the functionalization/modification of template surfaces to achieve favorable surface properties, the coating of the templates with designed materials or their precursors, possibly with post treatment to form compact shells, and the selective removal of the templates to obtain hollow structures. We have used monodispersive silica nanospheres as hard templates. These templates are

advantageous for diverse reasons including their narrow size distribution, availability in relatively large amounts and in a wide range of sizes from commercial sources, and simplicity of their synthesis using well-known formulations. Next, templates were functionalized with amino groups and coated with platinum seeds. Finally, platinum nanobubbles were made by etching the silica nanocores of $\text{SiO}_2\text{@Pt}$ core-shell nanospheres with $\text{HF}(\text{aq})$. The produced nanobubbles have been found to catalyze the degradation of rhodamine B efficiently with a remarkably reduced activation energy in the presence of KBH_4 compared with $\text{SiO}_2\text{@Pt}$ core-shell nanospheres.

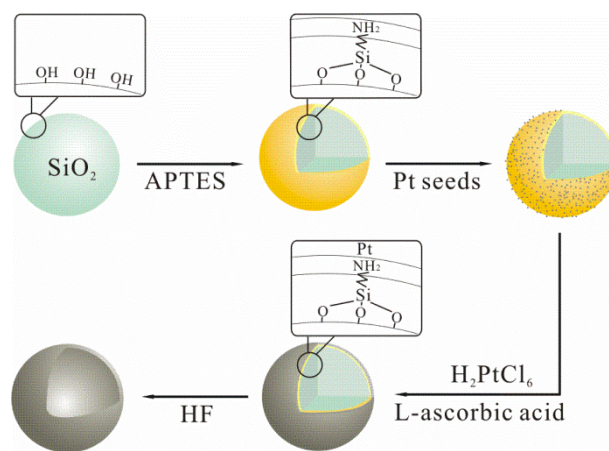


Figure 1-1. Schematic for the fabrication of platinum nanobubbles.

1.3. Experimental Section

Materials. H_2PtCl_6 (s, 99.995%), tetraethyl orthosilane(ℓ , TEOS, $\geq 99\%$), L-ascorbic acid(s), 25% NH_3 (aq), (3-aminopropyl)triethylsilane (ℓ , APTES, 98%), 50% HF(aq), 35% HCl(aq), polyvinylpyrrolidone(s, PVP, M.W. = 25000), NaBH_4 (s, 99.995%), rhodamine B(s), KBH_4 (s, $\geq 95\%$), and ethanol(ℓ) were used as purchased from Sigma-Aldrich. Ultrapure deionized water ($>17 \text{ M}\Omega \text{ cm}$) was obtained using a Millipore Milli-Q system.

Preparation of platinum nanocatalysts. All the synthetic processes of platinum nanocatalysts were taken place under ambient conditions. Monodispersive silica nanospheres were prepared from the sol-gel process of TEOS under base catalysis following the Stöber method [33]. 25.00 mL of ethanol, 4.50 mL of H_2O , 1.55 mL of TEOS, and a specified volume of 25% NH_3 (aq) were mixed and kept under vigorous stirring for 1 h. 0.40, 0.96, and 1.92 mL of 25% NH_3 (aq) were used to synthesize silica nanospheres, which were used later to fabricate platinum nanobubbles of 150, 250, and 400 nm, respectively, in an average outer diameter [34]. Produced silica nanospheres were centrifuged at 10,000 rpm for 10 min and redispersed in 31.45, 32.01, and 32.97 mL, respectively, of ethanol three times.

Platinum seeds were prepared by reducing H_2PtCl_6 in an aqueous PVP solution. 10.0 mg of H_2PtCl_6 (s) was dissolved in 10.00 mL of 35% HCl(aq), the

solution was mixed with 10.00 mL of 0.2 M NaBH₄(aq) and 10.00 mL of 0.3 g L⁻¹ PVP(aq) at once, and the solution was not stirred during the reaction [35]. The products were centrifuged at 10,000 rpm for 10 min and redispersed in 30.00 mL of ethanol three times.

For the modification of the surfaces of silica nanospheres with amino groups, 10.00 mL of silica nanospheres-dispersed ethanol was mixed with 5.00 mL of 1.0 M APTES in ethanol and kept under vigorous stirring for 2 h.

5.00 mL of platinum seeds was added to the above mixture solution and stirred for 1 h to attach platinum seeds on the surfaces of APTES-treated silica nanospheres. For the transformation of platinum seeds into platinum shells, 4.00 mL of 2 days-aged 10 mM H₂PtCl₆(aq) and 2.00 mL of the above mixture solution were mixed and stirred for 1 h. Then, 0.32 mL of 100 mM L-ascorbic acid(aq) was added and the reaction mixture was stirred for 1 h. Note that the molar concentration of platinum, [Pt], in the colloidal solution is 6.5 mM.

Platinum nanobubbles were prepared by reacting 1.00 mL of the colloidal solution containing SiO₂@Pt core-shell nanospheres with 10.00 mL of 0.5% HF(aq) for 2 min. Then, the products were centrifuged at 10,000 rpm for 10 min and redispersed in 1.00 mL of ethanol three times.

Characterization of platinum nanocatalysts. Transmission electron microscopic (TEM) images were obtained by a microscope (Carl Zeiss, LIBRA 120), and energy-dispersive X-ray (EDX) line-scanned elemental intensity

profiles and high-resolution TEM (HRTEM) images were measured by using a high-resolution microscope (FEI, Tecnai F20).

The catalytic properties of platinum nanocatalysts were measured by monitoring the reduction reaction of rhodamine B in the presence of KBH_4 . 0.40 mL of an ethanol colloidal solution containing platinum nanocatalysts was added into 0.90 mL of water and 1.70 mL of 20 μM rhodamine B(aq) contained in a polyphenyl cell having a path length of 10 mm and then 0.40 mL of 10 mM KBH_4 (aq) has been added rapidly. Then, the absorption spectral changes of rhodamine B were measured at scheduled intervals using a temperature-controllable spectrophotometer (Scinco, S-3000).

1.4. Results and discussion

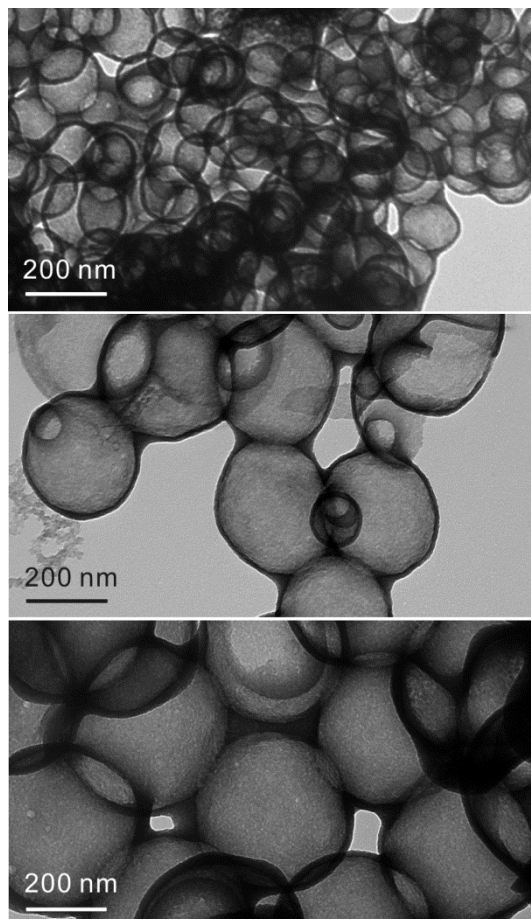


Figure 1-2. Transmission electron microscopy (TEM) images of platinum nanobubbles with average diameters of 150 (top), 320 (middle), and 420 nm (bottom).

Fig. 2 shows typical TEM images of platinum nanobubbles having average outer diameters of 150, 320, and 420 nm, illustrating that platinum nanobubbles have empty interiors because the TEM images of individual nanostructures are brighter in the central regions than in the edge regions. The sizes of platinum

nanobubbles were controlled by adjusting the template sizes of silica nanospheres, and the sizes of silica nanospheres were adjusted by varying the amounts of 25% $\text{NH}_3(\text{aq})$; as the larger volumes of the base were added, the bigger core templates of silica nanospheres were produced.

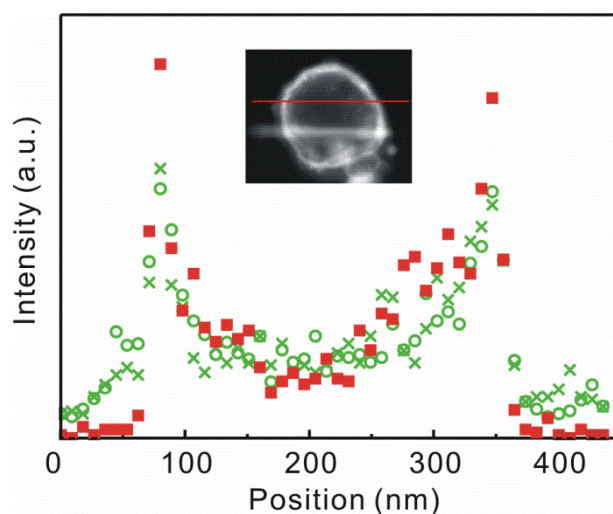


Figure 1-3. Area-normalized EDX elemental profiles of a platinum nanobubble scanned along the line in the HRTEM image of the inset. Squares indicate Pt while circles and crosses do Si and O, respectively.

The EDX line-scanned elemental profile of platinum measured along the indicated solid line of the platinum nanobubble in the HRTEM image of Fig. 3 exhibits two characteristic sharp peaks very well, indicating that the platinum nanobubble has a very hollow structure evidently. The insetted HRTEM image of Fig. 3 also displays well that the interior of the platinum nanostructure is vacant. The shapes and positions of two peaks of the Pt intensity profile are

similar to the respective ones of the Si and the O intensity profiles, indicating that the wall of a platinum nanobubble compositely consists of platinum and silica. However, a close examination of the elemental intensity profiles reveals that the thickness of the platinum shell is 20 nm whereas that of the silica shell is 30 nm. Furthermore, the elemental intensity profiles indicate that silica is also present on the outside of the platinum shell. These suggest that dissolved silica, which were produced during the core etching of SiO₂@Pt core-shell nanospheres with HF(aq), became precipitated again during the washing process to form solid silica, which was in contact with the platinum shell.

As illustrated in Fig. 1, platinum nanobubbles with uniform shell thickness have been prepared by etching the silica cores of SiO₂@Pt core-shell nanospheres. The sol-gel process of TEOS using base catalysts was employed to prepare nearly monodispersive silica nanospheres. Then, the hydroxyl groups on the surfaces of silica nanospheres were treated with APTES to form amino groups on the silica surfaces. We have found that the complete functionalization of the silica surfaces with a sufficient amount of APTES is essential for the proper coating of the silica surfaces with platinum seeds (Fig. S1 in the supporting Information). PVP-stabilized platinum seeds with diameters below 5 nm were attached to the surfaces of silica nanospheres. A coordination bond was formed between N and Pt to produce a silica-supported nitrogenous platinum complex (SiO₂-NH₂-Pt), which played an important role in attaching

platinum seeds to silica nanospheres [36]. Then, the platinum nanoseeds clustered on silica nanospheres were transformed into platinum shells via the reduction of newly added $\text{H}_2\text{PtCl}_6(\text{aq})$ with L-ascorbic acid to form $\text{SiO}_2@\text{Pt}$ core-shell nanospheres. The silica nanocores were excavated completely by reacting the core-shell nanospheres with an excess amount of $\text{HF}(\text{aq})$ to produce platinum nanobubbles. $\text{HF}(\text{aq})$ has been known to remove silica effectively through the stoichiometric reaction of $\text{SiO}_2(\text{s}) + 4\text{HF}(\text{aq}) \rightarrow \text{SiF}_4(\text{g}) + 2\text{H}_2\text{O}(\ell)$ [37]. Fig. S2 in the Supporting Information indicates that 2 min is a sufficiently long reaction time to remove the silica nanocores entirely; the reaction of the core-shell nanospheres with $\text{HF}(\text{aq})$ for 30 min has yielded broken platinum nanoshells.

We have explored the catalytic properties of platinum nanobubbles by monitoring time-dependent absorbance changes of rhodamine B degraded catalytically via the nanobubbles in the presence of KBH_4 (Fig. 4). For the sake of comparison, the catalytic performances of $\text{SiO}_2@\text{Pt}$ core-shell nanospheres have been also measured, revealing that the catalytic performances of platinum nanobubbles are much more efficient than those of $\text{SiO}_2@\text{Pt}$ core-shell nanospheres at the same concentration. The absorption of rhodamine B decreased much more rapidly in the presence of the nanobubbles (Fig. 4b-c) than in the presence of the core-shell nanospheres (Fig. 4a). Fig. 4b-c displays as well that the catalytic efficiency of platinum nanobubbles increases

extensively with the decrease of their sizes (see below).

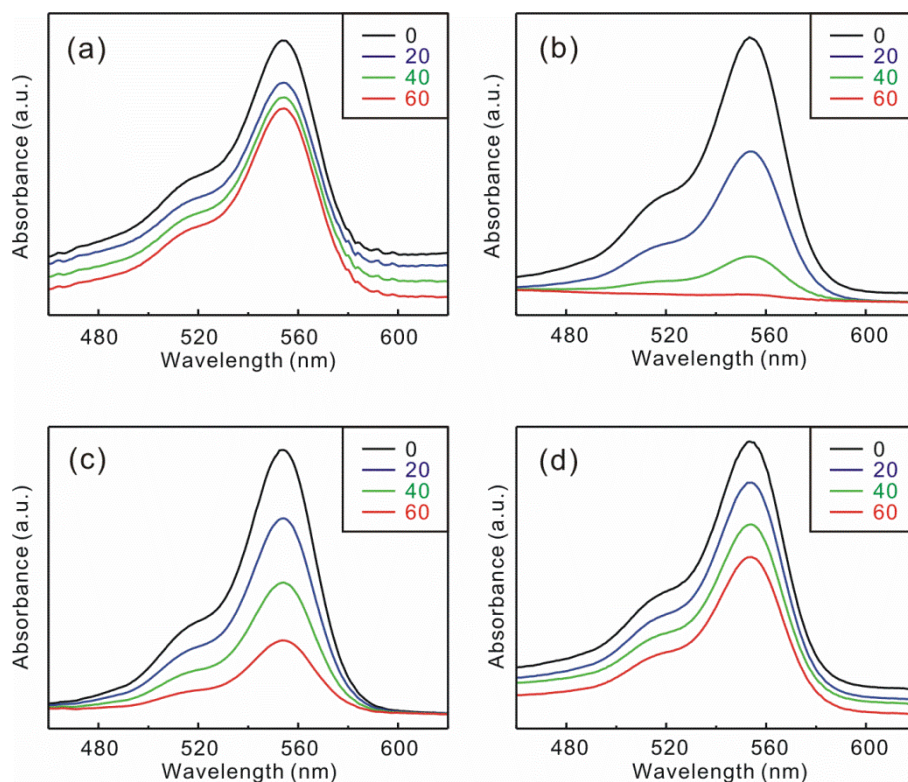


Figure 1-4. Absorption spectra at 30 °C of 10 μ M rhodamine B solutions in the presence of 1.2 mM KBH_4 after addition of (a) SiO_2 @Pt core-shell nanospheres having an average diameter of 150 nm (150C) and (b) platinum nanobubbles having average outer diameters of 150 nm (150H), (c) 320 nm (320H), and (d) 420 nm (420H), measured at elapsed times indicated in the units of min.

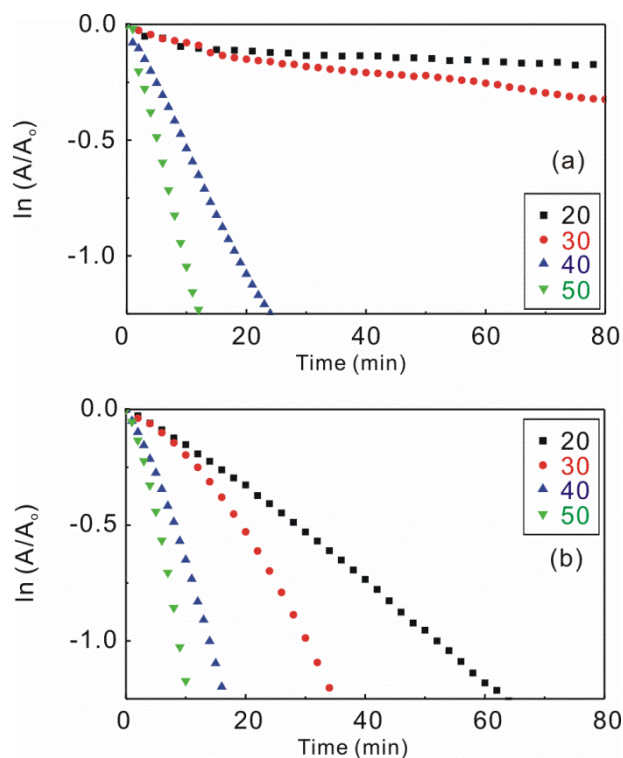


Figure 1-5. First-order kinetics, $\ln(A/A_0)$ vs t , for the catalytic degradation of $10 \mu\text{M}$ rhodamine B via nanocatalysts of (a) 150C and (b) 150H in the presence of 1.2 mM KBH_4 at temperatures indicated in the units of Celsius degrees.

The temperature-dependent first-order degradation kinetic profiles of rhodamine B via platinum nanocatalysts in the presence of KBH_4 in Fig. 5 have been employed to extract the observed degradation rate constants (k_{obs}); the pseudo-linear plots of $\ln(A/A_0) = -kt$ [38], where A is the optical density at 554 nm of rhodamine B and t is the time of the reaction, yield k_{obs} shown in Table 1. The catalytic rate constant (k_{cat}) of a platinum nanocatalyst can be obtained by subtracting the degradation rate constant (k_0) of rhodamine B in the absence of any nanocatalysts from k_{obs} ; $k_{\text{cat}} = k_{\text{obs}} - k_0$. Note that rhodamine B in the

presence of nanocatalysts hardly decomposes in the absence of KBH_4 , suggesting the decolorization of rhodamine B is not due to its adsorption to nanocatalysts [39]. The k_{cat} of 150H, which is larger by 8 times than the reported value at 25 °C [39], has been found to be larger by 23 times than that of 150C, suggesting that the excavation of the silica cores of the 150C nanocatalysts enhances the catalytic efficiency enormously. Table 1 also displays that the catalytic efficiency of platinum nanobubbles increases greatly indeed with the decrease of their sizes. The temperature dependence of the kinetic profiles in Fig. 5b is much smaller than that in Fig. 5a, implying that the excavation of 150C reduces the activation energy of k_{cat} substantially (see below).

Table 1-1. Comparison of rate constants, frequency factors, activation energies, and activation entropies for the catalytic degradation of rhodamine B via platinum nanocatalysts in the presence of KBH_4 .

Nanocatalyst	k_{obs} at 30 °C (min^{-1})	k_{cat} at 30 °C (min^{-1})	Frequency factor (min^{-1})	Activation energy (kcal mol^{-1})	Entropy of activation ($\text{cal mol}^{-1} \text{K}^{-1}$)
a	0.0028	0			
150C	0.0041	0.0013	3.9×10^{19}	30.5	- 14.2
150H	0.032	0.030	1.6×10^6	10.7	- 29.6
320H	0.021	0.018	3.1×10^8	14.5	- 17.5
420H	0.0090	0.0062	1.0×10^9	15.7	- 15.6

^a In the absence of any nanocatalysts.

The frequency factor of the catalytic degradation of rhodamine B via the 150C nanocatalyst extracted from an Arrhenius plot [38] of Fig. 6a is the

highest ever reported for this reaction (Table 1) [40,41]. However, the k_{cat} of 150C is rather small due to its large activation energy. The frequency factor and the activation energy of the catalytic degradation via 150H in Table 1 indicate that the excavation of the $\text{SiO}_2\text{@Pt}$ core-shell nanospheres reduces the activation energy severely and the frequency factor drastically. This then suggests that the catalysis mechanism of platinum nanobubbles is completely different from that of the core-shell nanospheres (see below). Fig 6a and Table 1 also reveal that both the frequency factor and the activation energy increase gradually with the size increase of platinum nanobubbles. This hints that the catalysis mechanism of platinum nanobubbles remains the same regardless of their sizes within our studied range; the catalytic reaction takes place within the nanocavities of platinum nanobubbles. The decrease of k_{cat} , resulting mainly from the increase of the activation energy, with size increase has been attributed to the reduction of the nanoreactor confinement effect of platinum nanobubbles [41]. Eyring plots [42] have revealed that the entropy of activation for 150H is much larger than that for 150C. Furthermore, the entropy of activation decreases with the size increase of platinum nanobubbles. These also support that the catalytic reaction via platinum nanobubbles takes place within their nanocages whereas the reaction via $\text{SiO}_2\text{@Pt}$ core-shell nanospheres does on their surfaces.

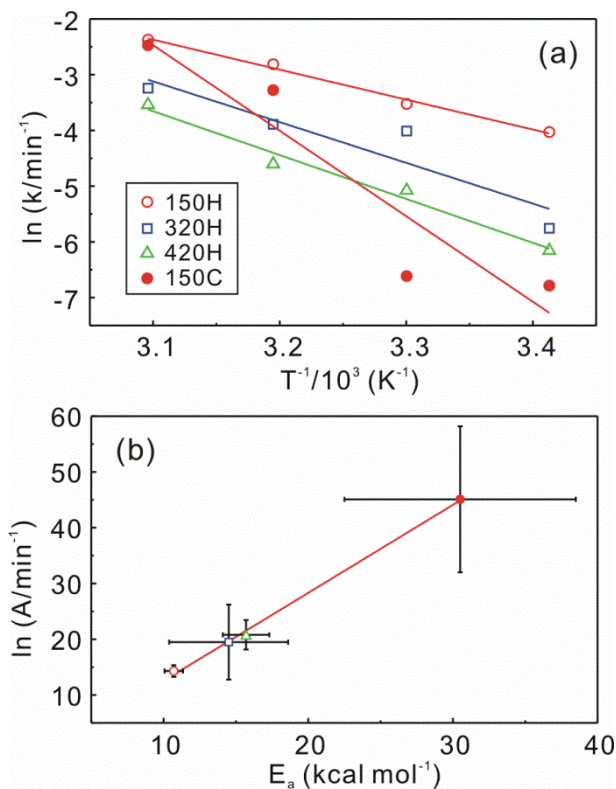


Figure 1-6. (a) Arrhenius plots for the catalytic degradation reaction of 10 μM rhodamine B in the presence of 1.2 mM KBH_4 via platinum nanocatalysts indicated inside. (b) The compensation law plot of the activation energies and the frequency factors obtained from the slopes and the intercepts, respectively, of the Arrhenius plots.

Fig 6(b) shows the existence of a good compensation relation in the catalytic systems of our platinum nanostructures. The following empirical linear relationship has been found to hold between the frequency factor (A) and the activation energy (E_a); $\ln A = \alpha + E_a / (RT_\theta)$ where α is a constant and T_θ is called the fictitious isokinetic temperature, at which the rates on all the nanocatalysts become equal [43,44]. In our systems, T_θ has been found to be

319 K. It is considered that a catalyst such as 150C has a large concentration of active sites where the reaction requires high E_a , while another catalyst such as 150H has a small concentration of active sites that have low E_a for the same catalytic reaction.

Because catalysis by metals is a surface phenomenon, small sizes of nanocatalysts with a large fraction of the atoms exposed to environment have high catalytic properties [45]. The catalytic degradation mechanism of organic pollutants such as rhodamine B in the presence of our platinum nanocatalysts and KBH_4 could be explained as follows. Rhodamine B is electrophilic and BH_4^- is nucleophilic with respect to platinum nanocatalysts. Thus, the nucleophile BH_4^- can donate electrons to platinum nanocatalysts, and the electrophile rhodamine B can capture electrons from the platinum nanocatalysts; platinum nanocatalysts serve as electron relays for the degradation reaction of rhodamine B in an aqueous KBH_4 solution [46]. The catalytic electron relays occur on the outer metallic surfaces of the core-shell nanospheres. However, they take place with much smaller E_a in the nanocavity surfaces of the platinum nanobubbles. Thus, we suggest that the nanoreactor confinement effect of the platinum nanobubble has expedited electron relays from BH_4^- to rhodamine B tremendously by reducing E_a extensively. The size dependence of the catalytic activation energy (E_a) could be obtained from the following relation; $E_a / E_{a,\infty} = T_m / T_{m,\infty} = 1 - \alpha_{\text{shape}} / D$ [47]. T_m is the melting

temperature of the nanostructure, α_{shape} is the shape parameter defined as $\alpha_{\text{shape}} = A D (\gamma_s - \gamma_l) / (V \Delta H_{m,\infty})$, D is the size of the structure, and A and V are the surface area and volume of the nanostructure, respectively. $\Delta H_{m,\infty}$ is the bulk melting enthalpy and γ_s and γ_l are the surface energy in the liquid and solid phases, respectively. It means that the catalytic activation energy increases with size increase as confirmed with our experimental data in Table 1.

1.5. Conclusions

Platinum nanobubbles having a uniform shell thickness of 20 nm with average outer diameters of 150, 320, and 420 nm have been successfully prepared by etching the cores of SiO₂@Pt core-shell nanospheres with HF(aq). The sizes of platinum nanobubbles have been controlled by adjusting the template sizes of silica nanospheres with varying the amount of NH₃(aq). Platinum nanobubbles have been found to catalyze the degradation of organic pollutant dyes such as rhodamine B efficiently in the presence of KBH₄ compared with SiO₂@Pt core-shell nanospheres. We have investigated the catalytic mechanism of the nanocatalysts by monitoring various kinetic parameters such as rate constants, activation energies, frequency factors, and entropies of activation. The temperature dependence of the catalytic degradation rate constants via platinum nanobubbles is much smaller than that via SiO₂@Pt core-shell nanospheres, implying that the catalysis mechanisms of the two different nanocatalysts are completely different. The catalytic activation energy of the degradation of rhodamine B has been found to decrease with the size decrease of platinum nanobubbles. These suggests that the catalytic reaction via platinum nanobubbles occurs within their nanocages, whereas the reaction via SiO₂@Pt core-shell nanospheres does on their surfaces. The existence of a good compensation effect between activation energies and frequency factors has been

evidenced for the platinum nanocatalysts, revealing that the isokinetic temperature is 319 K.

1.6. Acknowledgments

This work was supported by research grants through the National Research Foundation (NRF) of Korea funded by the Ministry of Education, Science, and Technology (2011-0028981 and 2012-006345). D.J.J. is also thankful to the SRC program of NRF (2007-0056331).

1.7. Supporting Information

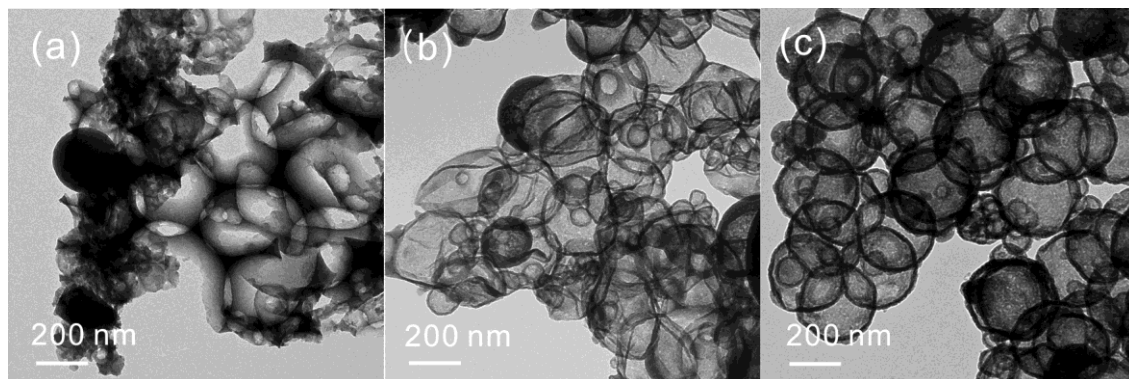


Fig. S1. TEM images of platinum nanobubbles prepared with (a) 1.25 mL, (b) 2.50 mL, and (c) 5.00 mL of APTES.

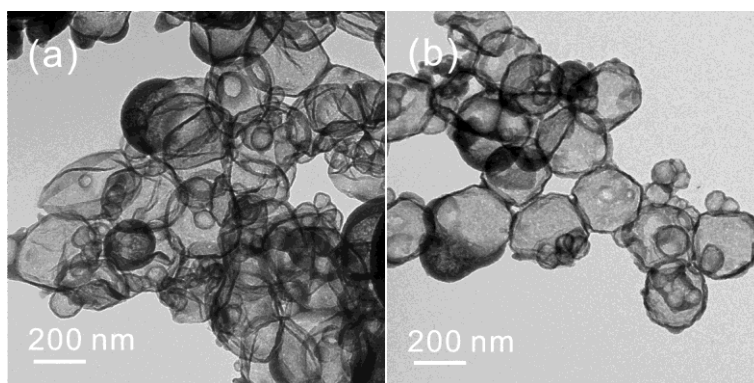


Fig. S2. TEM images of platinum nanobubbles prepared by excavating the cores of SiO₂@Pt core-shell nanospheres with 10 mL of 0.5% HF(aq) for (a) 2 min and (b) 6 min.

1.8. References

- [1] J. Lee, S. Mahendra, P.J.J. Alvarez, *ACS Nano* 4 (2010) 3580-3590.
- [2] H. Yoo, J. Sharma, H.-C. Yeh, J.S. Martinez, *Chem. Commun* 46 (2010) 6813-6815.
- [3] Y.H. Kim, J.-Y. Kim, D.-J. Jang, *J. Phys. Chem. C* 116 (2012) 10296-10302.
- [4] H.-B. Kim, D.-J. Jang, *Cryst. Eng. Comm.* 14 (2012) 6946-6951.
- [5] J.-Y. Kim, H. Jeong, D.-J. Jang, *J. Nanopart. Res.* 13 (2011) 6699-6706.
- [6] S.J. Kim, C.S. Ah, D.-J. Jang, *Adv Mater.* 19 (2007) 1064-1068.
- [7] M.R. Kim, J.-Y. Kim, S.J. Kim, D.-J. Jang, *Appl. Catal. A: Gen.* 393 (2011) 317-322.
- [8] T.K. Sau, A.L. Rogach, F. Jäckel, T.A. Klar, J. Feldmann, *Adv. Mater.* 22 (2010) 1805-1825.
- [9] C. Noguez, *J. Phys. Chem. C* 111 (2007) 3806-3819.
- [10] S.J. Kim, D.-J. Jang, *Mater. Lett.* 62 (2008) 4500-4502.
- [11] M.A. Mahmoud, M.A. El-Sayed, *Langmuir* 28 (2012) 4051-4059.
- [12] P.K. Jain, X.H. Huang, I.H. El-Sayed, M.A. El-Sayed, *Acc. Chem. Res.* 41 (2008) 1578-1586.
- [13] J. Gao, X. Ren, D. Chen, F. Tang, J. Ren, *Scripta Mater.* 57 (2007) 687-690.

- [14] H.M. Lu, X.K. Meng, *J. Phys. Chem. C* 114 (2010) 1534-1538.
- [15] H. Atae-Esfahani, Y. Nemoto, L. Wang, Y. Yamauchi, *Chem. Commun.* 47 (2011) 3885-3887.
- [16] L. Kuai, S. Wang, B. Geng, *Chem. Commun.* 47 (2011) 6093-6095.
- [17] J. Wang, Z. Jiang, Z. Zhang, Y.P. Xie, X.F. Wang, Z.Q. Xing, R. Xu, X.D. Zhang, *Ultrason. Sonochem.* 15 (2008) 768-774.
- [18] Q. Tang, X. Huang, Y. Chen, T. Liu, Y. Yang, *J. Mole. Catal. A: Chem.* 301 (2009) 24-30.
- [19] P. Huber, B. Carré, *BioRes.* 7 (2012) 1366-1382.
- [20] R. Narayanan, M.A. El-Sayed, *Nano Lett.* 4 (2004) 1343-1348.
- [21] Y. Li, J. Petroski, M.A. El-Sayed, *J. Phys. Chem. B* 104 (2000) 10956-10959.
- [22] T. Herricks, J. Chen, Y. Xia, *Nano Lett.* 4 (2004) 2367-2371.
- [23] R. Krishnaswamy, H. Remita, M. Inpéror-Clerc, C. Even, P. Cavidson, B. Pansu, *Chem. Phys. Chem.* 7 (2006) 1510-1513.
- [24] Y.-J. Han, J.M. Kim, G.D. Stucky, *Chem. Mater.* 12 (2000) 2068-2069.
- [25] Y. Luo, S.K. Lee, H. Hofmeister, M. Steinhart, U. Gösele, *Nano Lett.* 4 (2004) 143-147.
- [26] Y. Song, Y. Yang, C.J. Medforth, E. Pereira, A.K. Singh, H. Xu, Y. Jiang, C.J. Brinker, F.V. Swol, J.A. Shelnutt, *J. Am. Chem. Soc.* 126 (2004) 635-645.
- [27] H. Wang, Y. Song, C.J. Medforth, J.A. Shelnutt, *J. Am. Chem. Soc.* 128

(2006) 9284-9285.

[28] M.R. Kim, D.K. Lee, D.-J. Jang, *Appl. Catal. B: Env.* 103 (2011) 253-260.

[29] X.W. Lou, L.A. Archer, Z. Yang, *Adv. Mater.* 20 (2008) 3987-4019.

[30] Y. Yin, R.M. Rioux, C.K. Erdonmez, S. Hughes, G.A. Somorjai, A.P. Alivisatos, *Science* 304 (2004) 711-714.

[31] H.G. Yang, H.C. Zeng, *J. Phys. Chem. B* 108 (2004) 3492-3495.

[32] F. Caruso, *Chem. Eur. J.* 6 (2000) 413-419.

[33] W. Stöber, A. Fink, E. Bohn, *J. Colloid Interface Sci.* 26 (1968) 62-69.

[34] J.W. Kim, L.U. Kim, C.K. Kim, *Biomacromolecules* 8 (2007) 215-222.

[35] V.R. Calderone, J. Schütz-Widoniak, G.L. Bezemer, G. Bakker, C. Steurs, A.P. Philipse, *Catal. Lett.* 137 (2010) 132-140.

[36] J. Li, C. Yang, L. Zhang, T. Ma, *J. Organomet. Chem.* 696 (2011) 1845-1849.

[37] B. Liu, W. Zhang, H. Feng, X. Yang, *Chem. Commun.* 47 (2011) 11727-11729.

[38] N.S. Langeroodi, *Russ. J. Phys. Chem. A* 86 (2012) 628-631.

[39] M.A. Mahmoud, M.A. El-Sayed, *NanoLett.* 11 (2011) 946-953.

[40] J. Zeng, Q. Zhang, J. Chen, Y. Xia, *Nano Lett.* 10 (2010) 30-35.

[41] M.A. Mahmoud, F. Saira, M.A. El-Sayed, *Nano Lett.* 20 (2010) 3764-3769.

[42] K.D. Zimmer, R. Shoemaker, R.R. Ruminski, *Inorg. Chim. Acta* 359

(2006) 1478-1484.

[43] T. Bligaard, K. Honkala, A. Logadottir, J.K. Norskov, S. Dahl, C.J.H.

Jacobsen, J. Phys. Chem. B 107 (2003) 9325-9331.

[44] G.A. Somorjai, Introduction to Surface Chemistry and Catalysis, John Wiley & Sons, Inc., USA, 1994.

[45] Z. Xu, F.-S. Xiao, S.K. Purnell, O. Alexeev, S. Kawi, S.E. Deutsch, B.C. Gates, Nature 372 (1994) 346-348.

[46] Z. Deng, M. Chen, L. Wu, J. Phys. Chem. C 111 (2007) 11692-11698.

[47] G. Guisbiers, G. Abudukelimu, D. Hourlier, Nano Res. Lett. 6 (2011) 396(1)-(5).

Chapter 2. Surface Plasmon Resonances of Pt Nanobubbles and Their Characterization

2.1. Abstract

Pt nanostructures with the average outer diameter of 148 nm and shell thickness of 11 nm have been synthesized via hard templating method and we have examined the solvent effects on the optical extinction spectra. The surface-plasmon bands of the Pt nanostructures have investigated by performing the extended Mie theory calculation and this theory for the nanoshell geometry quantitatively accounts for the observed Pt plasmon resonance. The surface plasmon resonance of the Pt nanostructures is sensitive to the relative dimensions of the core diameter, shell thickness, and dielectric constant of surrounding. Also, the experimental spectra for the Pt nanostructures dispersed in water agree well with the calculated spectra.

2.2. Introduction

Nanocomposite materials based on the noble metal nanoparticles have attracted increasing attention thanks to their intriguing chemico-physical properties that can be tailored as a function of their sizes and shapes [1]. Especially, the core-shell composite nanospheres with a dielectric solid (e.g., silica, polystyrene) covered by a metallic nanoshells have been studied extensively, since they have great potential applications in catalysis, chemical and biological sensing, optoelectronics, photonic crystals, the plasmonics and surface-enhanced Raman scattering-based analytical devices, and so forth [2-6].

Noble metal based nanostructures exhibit the exciting properties unique dependent on the size and shape within the nano-size regime. The most interesting property of these nanostructures is the optical field enhancements resulting in the strong scattering and absorption of lights. The enhancement in the optical properties of noble metal nanostructures arises from resonant oscillation of their free electrons in the presence of light, known as localized surface plasmon resonance (LSPR) [7-11]. For example, solid gold nanoparticles have a strong optical absorption at 520 nm, and silver nanoparticles have a resonance at 390 nm [12].

The surface plasmon resonance can be understood with the Mie scattering theory [13,14] and this theory is the solution of Maxwell's equations in

spherical coordinates with boundary conditions appropriate for a sphere (allowing us to solve Laplace's equation for the electric potential) [15]. Although the general Mie scattering solutions for a spherical particle consisting of concentric layers has been known for decades [16], it was recently theoretically established that a configuration consisting of a metallic shell and dielectric core should result in a particle with a plasmon-derived optical resonance variable over large regions of the electromagnetic spectrum [17]. To determine the extinction spectrum of nanostructures using the theory, the electromagnetic fields of the incident wave, scattered wave and the wave inside the particle are expressed as the sum of a series of vector spherical harmonic basis function. The electromagnetic fields must then satisfy Maxwell's boundary conditions of continuity at the junction between the nanostructure and the embedding medium. Mie scattering theory is exact and it accounts for field-retardation effect that becomes significant for particles whose sizes are comparable to the wavelength of light [18, 19].

In this paper, we have synthesized Pt nanostructures via hard templating method [20] involving the four or five major steps: (1) preparation of the SiO₂ hard templates; (2) modification of the SiO₂ surfaces with amino groups; (3) coating the SiO₂ templates with the Pt seeds; (4) transformation from the Pt clusters topped on SiO₂ surfaces to the Pt nanoshells; and (5) etching of SiO₂ hard templates with aqueous HF. After the synthesis, we have examined the

solvent effects on the optical extinction spectra. The Surface-plasmon bands of the Pt nanostructures have been investigated by performing the Mie theory calculation and the experimental spectra for the platinum nanostructures dispersed in water agree well with the calculated spectra.

2.3. Experimental Section

For synthesis of monodispersive SiO₂ hard templates, 25.00 mL of ethanol(l), 4.50 mL of deionized water(> 17MΩ), 0.40 mL of 25 % ammonia solution(aq), and 1.55 mL of tetraethyl orthosilicate(l) were mixed and kept under stirring for 1 hour. SiO₂ hard templates were centrifuged with 10,000 rpm for 10 min and redispersed in 31.45 mL of ethanol three times [21,22]. Platinum seeds were prepared by mixing of 10.0 mg of H₂PtCl₆(s) in 10.00 mL of 35% HCl(aq), 10.00 mL of 0.2 M NaBH₄(aq), and 10.00 mL of 0.3 g L⁻¹ PVP(aq) at once, and the solution was not stirred during the reaction. The products were centrifuged at 10,000 rpm for 10 min and redispersed in 30.00 mL of ethanol three times [23]. For the modification of the surfaces of SiO₂ hard templates with amino groups, 10.00 mL of SiO₂ hard templates-dispersed in ethanol and 5.00 mL of 1.0 M APTES were mixed and kept under stirring for 2 h. Then, 5.00 mL of Pt seeds solution was added and stirred for 1 h to attach the Pt seeds on the SiO₂ hard templates. For the transformation of platinum seeds into platinum shells, 4.00 mL of 2 days-aged 10 mM H₂PtCl₆(aq) and 2.00 mL of the above mixture solution were mixed and stirred for 1 h and 0.32 mL of 100 mM L-ascorbic acid(aq) was added and stirred for 1 h [24]. Finally, 10.00 mL of aqueous HF and 1.00 mL of above solution were mixed and stirred 2 min [25]. The products were centrifuged at 10,000 rpm for 10 min and redispersed in 1.00 mL of

ethanol three times.

Transmission electron microscopic (TEM) images were obtained by microscope (Carl Zeiss, LIBRA 120), and the extinction spectra of Pt nanostructures dispersed in water, ethanol, and dibutyl ether were measured by UV-vis spectrophotometer (Scinco, S-3000).

2.4. Results and discussion

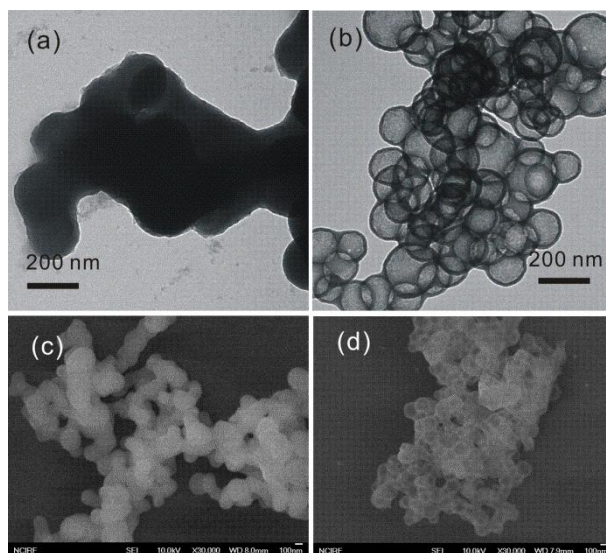


Figure 2-1. Transmission electron microscopy (TEM) images of (a) SiO₂@Pt core-shell nanospheres and (b) Pt nanobubbles. Scanning electron microscopy (SEM) images of (c) SiO₂@Pt core-shell nanospheres and (d) Pt nanobubbles, respectively.

Fig. 1 shows typical TEM images and SEM images of Pt nanostructures. SiO₂@Pt core-shell nanospheres are agglomerated in Fig. 1(a), but we can confirm that the SiO₂@Pt core-shell nanostructures have the sphere morphologies through the SEM image of Fig. 1(c). Fig. 1(b) shows the Pt nanobubbles having empty interiors, because the TEM image of individual nanospheres is darker in the shell regions than in the central regions. The central region of individual Pt nanobubbles in Fig. 1(d) is brighter than the SEM image of SiO₂@Pt core-shell nanospheres in Fig. 1(c)

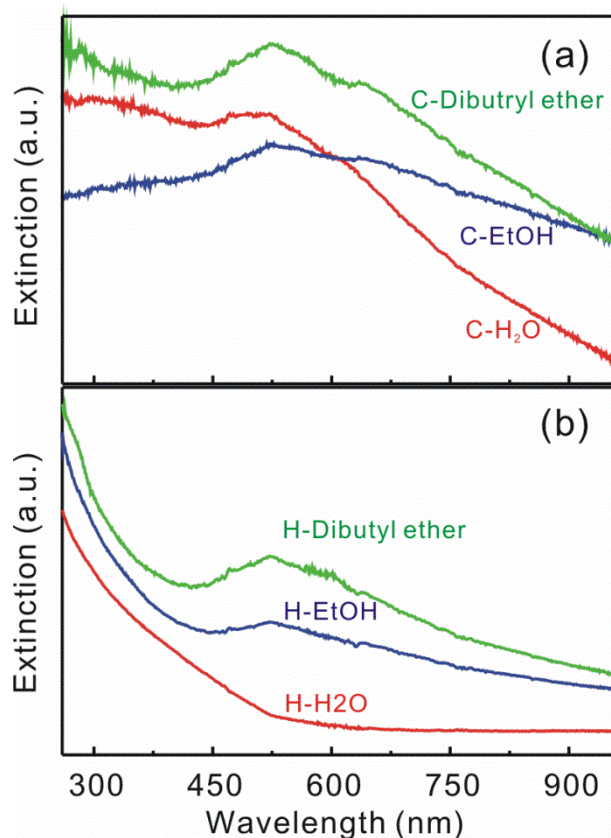


Figure 2-2. Representative experimental extinction spectra of (a) SiO₂@Pt core-shell nanospheres and (b) Pt nanobubbles dispersed in H₂O (red), EtOH (blue), and dibutyl ether (green).

Fig. 2 shows the UV-vis extinction spectra of the Pt nanostructures dispersed in three different solvent. We can see that the plasmon bands in UV-vis extinction spectra of the Pt nanobubbles exhibits an increasement towards the shorter wavelength, whereas the extinction spectra of the SiO₂@Pt core-shell nanospheres shows overall increased intensity compared with the Pt nanobubbles. We suggest that this phenomenon is due to existence of SiO₂ nanocores. We also confirmed that the surface plasmon resonance of the

platinum nanostructures is a very sensitive to the surrounding medium.

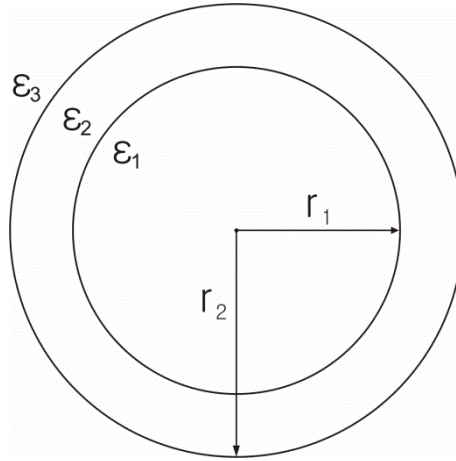


Figure 2-3. Geometry of the nanoshell structures: ϵ_n ($n = 1, 2, 3$) is the dielectric constant of the core, shell, and surrounding medium. r_1 and r_2 are radius of core and core-shell nanospheres, respectively.

Conceptually, the extension of the Mie theory to a metallic shell is quite simple: one must simply specify the boundary conditions at one additional interface [12]. The core-shell system depicted in Fig. 3 has been studied with the Mie theory, and expressions for the polarizability and the extinction cross section of core-shell particles have been derived. Furthermore, the quasi-static equations are useful in the calculation of nonlinear optical effects in nanoshells [26].

The core has radius r_1 and dielectric function ϵ_1 , the shell has a thickness $r_2 - r_1$ and dielectric function ϵ_2 , and the surrounding medium has dielectric function

$\epsilon_3 = n_0^2$, where n_0 is the refractive index of the surrounding medium in Fig. 3. It is important note that, each dielectric functions of ϵ_n ($n=1,2,3$) having real and imaginary frequency-dependent components can be written as $\epsilon(\omega) = \epsilon_r + i\epsilon_i$, where ω is the angular frequency of the light.

Especially, the optical response of metal shell regions is dominated by two contributions of the electrons to the dielectric function. ϵ_r corresponds to the conduction electrons. It is associated to intraband optical processes (electrons and holes belonging to the same band) that can be described in first approximation by a Drude dielectric function. ϵ_i corresponds to interband optical processes which can be described as

$$\epsilon(\omega) = \epsilon_r + i\epsilon_i = \epsilon_b(\omega) - \frac{\omega_p^2/\omega^2}{1 + \frac{1}{\omega^2\tau^2}} + i \frac{\omega_p^2/\omega^2}{\omega\tau(1 + \frac{1}{\omega^2\tau^2})} \quad (1)$$

where ω_p donates the plasmon frequency of the bulk metal, τ is the relaxation time and ω is the frequency of electromagnetic wave.

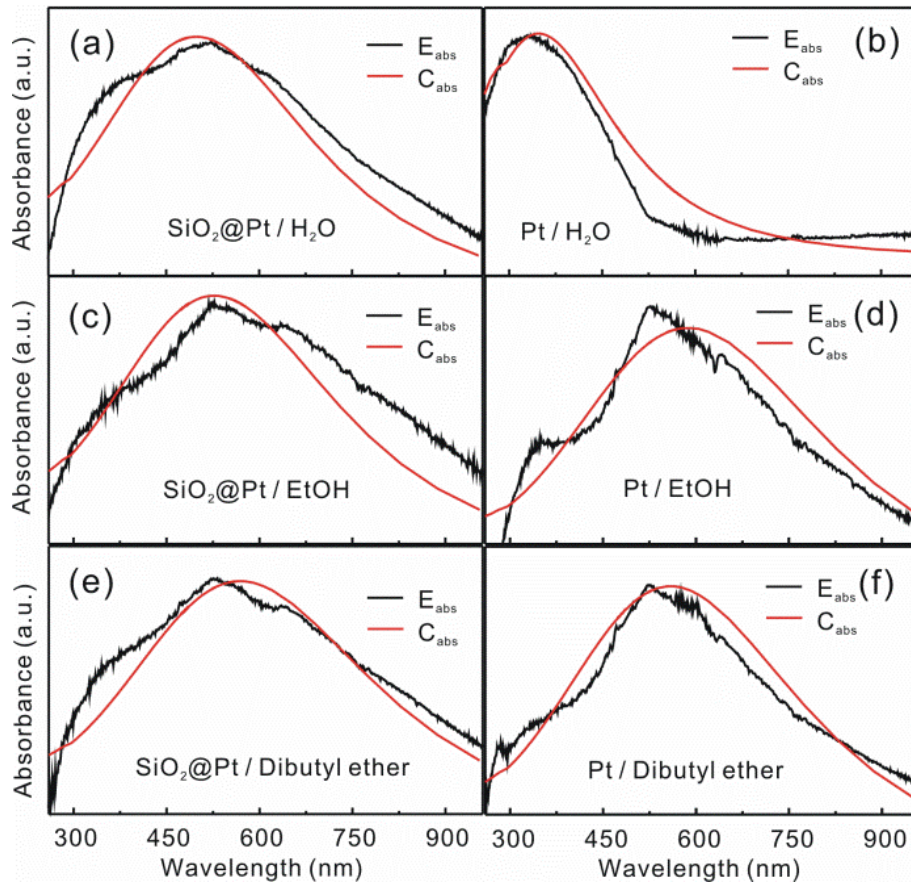


Figure 2-4. Extended Mie theory calculations (red) and experimental data (black) of the absorption efficiency spectra. (a,c,e) SiO₂@Pt core-shell nanospheres and (b,e,f) Pt nanobubbles having a uniform thickness of 20 nm with average outer diameters of 148 nm were dispersed in water (top), ethanol (middle), and dibutyl ether (bottom), respectively.

We have obtained the scattering-removed absorption spectra of Fig. 4 by subtracting $(c_1 / \lambda^4 + c_2)$ [27], where c_1 and c_2 are arbitrary constants, from the extinction spectra of Fig. 3. According to the quasi-static theory of nanoshells, the absorption (σ_{abs}) and the scattering cross (σ_{sca}) section obtained from the Mie theory calculation can be given by

$$\sigma_{\text{abs}} = \frac{k}{\varepsilon_0} \text{Im}(\alpha) \quad (2)$$

$$\sigma_{\text{sca}} = \frac{k}{6\pi\varepsilon_0^2} k^4 |\alpha|^2 \quad (3)$$

$$k = 2\pi\sqrt{\varepsilon_3} / \lambda \quad (4)$$

where ε_0 vacuum permittivity ($8.85 \times 10^{-12} \text{ C}^2 \text{ J}^{-1} \text{ m}^{-2}$), and α is the polarizability derived from Laplace's equation. α is give as follow [28]:

$$\alpha = 4 \pi \varepsilon_0 r_2^3 \frac{(\varepsilon_2 - \varepsilon_3)(\varepsilon_1 + 2\varepsilon_2) + \left(\frac{r_1}{r_2}\right)^3 (\varepsilon_1 - \varepsilon_2)(\varepsilon_3 + 2\varepsilon_2)}{(\varepsilon_2 + 2\varepsilon_3)(\varepsilon_1 + 2\varepsilon_2) + \left(\frac{r_1}{r_2}\right)^3 (2\varepsilon_2 - 2\varepsilon_3)(\varepsilon_1 - \varepsilon_2)} \quad (5)$$

Table 2-1. Dielectric constants of each regions of nanostructures. The number in the bracket is numerical value used for the calculation.

Solvent	Core-shell	Core-shell	Hollow	Hollow
	ε_1	ε_3	ε_1	ε_3
H ₂ O	2.10 (2.10)	1.76 (1.75)	1.76 (0.93)	1.76 (0.93)
EtOH	2.10 (2.10)	1.85 (2.00)	1.85 (2.45)	1.85 (2.45)
Dibutyl ether	2.10 (2.10)	1.95 (2.45)	1.95 (2.25)	1.95 (2.25)

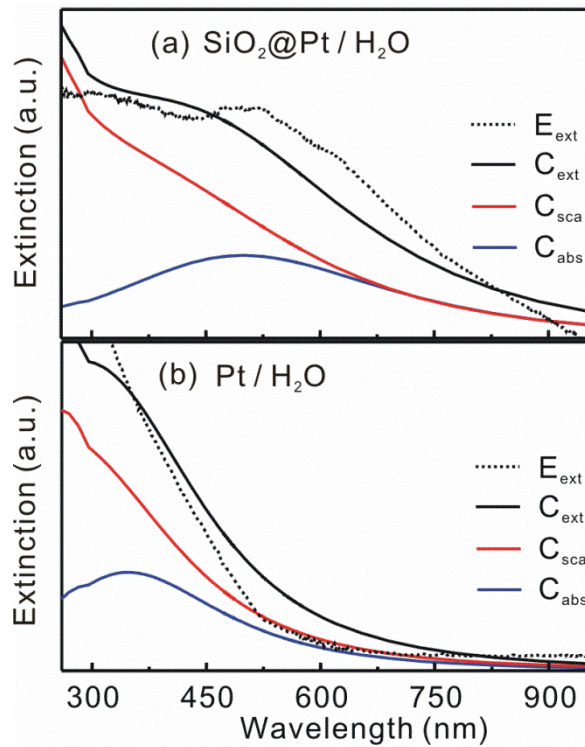


Figure 2-5. Mie theory calculations (solid line) of absorption (blue), scattering (red), and extinction (black) and experimental data (dotted line). (a) $\text{SiO}_2\text{@Pt}$ core-shell nanospheres and (b) Pt nanobubbles are dispersed in water, respectively.

Fig. 5 Shows the calculated absorption, scattering, and extinction efficiency for the platinum nanoshells with 63 nm of inner radius and 74 nm of outer radius. We have used a dielectric constant of 2.10 for the core material corresponding to SiO_2 and 1.75, 2.00, and 2.45 for the surrounding medium in Fig. 5(a). The dielectric constant of the surrounding medium used in calculation is quietly different from the real dielectric constants. Because the solvent is not completely pure, the number used in the calculation is a proper value. We can

see the small peak of experimental data in Fig. 5(a) at 500 nm and this peak is corresponding to the calculated absorption spectrum having a maximum wavelength at 500 nm. The plasmon bands in UV-vis extinction spectra of the SiO₂@Pt nanospheres exhibits an increasement towards the shorter wavelength and it is corresponding to the calculated scattering spectrum of Fig. 5(a). We can see the same tendency in case of Pt nanobubbles in Fig. 5(b).

These equations have been used extensively to explain the absorption spectra of small metallic nanostructures in a qualitative as well as quantitative manner. As a function of increasing size, contributions from higher-order multipoles and retardation effects become important [29-31]. Although the sizes of Pt nanostructures used in this experiment are slightly larger than theoretical sizes, the surface plasmon resonances of platinum have been studied at no time, so it is a very meaningful discussion in this regard.

2.5. Conclusions

We have successfully synthesized the Pt-based core-shell nanospheres with 74 nm silica core diameter and 11 nm platinum shell thickness, and obtained the hollow nanobubbles via the acid etching of SiO₂ nanocores. We have calculated the surface plasmon resonance of SiO₂@Pt core-shell nanospheres and Pt nanobubbles via the extended Mie theory by changing the dielectric constants of surrounding medium and we have compared it with the experimental data. The calculated extinction spectra considerably agree with the experimental data in case of water as solvent.

2.6. References

- [1] L. Armelao, D. Barreca, G. Bottaro, A. Gasparotto, S. Gross, C. Maragon, E. Tondello, *Coord. Chem. Rev.* **2006**, 250, 1294.
- [2] Z. Deng, M. Chen, L. Wu, *J. Phys. Chem. C* **2007**, 111, 11692.
- [3] O. Siiman, A. Burshteyn, *J. Phys. Chem B* **2000**, 104, 9795.
- [4] C. Graf, A. Van Blaaderen, *Langmuir* **2002**, 18, 524.
- [5] W. Wang, S.A. Asher, *J. Am. Chem. Soc.* **2001**, 123, 12528.
- [6] Z. Jiang, C.Y. Liu, *J. Phys. Chem. B* **2003**, 107, 12411.
- [7] P.K. Jain, X. Huang, I.H. El-Sayed, *Acc. Chem. Rev.* **2008**, 41, 1578.
- [8] C. Noguez, *J. Phys. Chem. C* **2007**, 111, 3806.
- [9] S.J. Kim, D.-J. Jang, *Mater. Lett.* **2008**, 62, 4500.
- [10] M.A. Mahmoud, M.A. El-Sayed, *Langmuir* **2012**, 28, 4051.
- [11] J. Gao, X. Ren, D. Chen, F. Tang, J. Ren, *Scripta Mater.* **2007**, 57, 687.
- [12] R.D. Averitt, S.L. Westcott, N.J. Halas, *J. Opt. Soc. Am. B* **1999**, 16, 1824.
- [13] G. Mie, *Ann. Phys.* **1908**, 25, 377.
- [14] U. Kreibig, M. Vollmer, *Optical properties of Metal Clusters*, Springer, Berlin, 1995.
- [15] S. Link, M.A. El-Sayed, *Rev. Phys. Chem.* **2000**, 19, 409.
- [16] A.L. Aden, J.Kerker, *J. Appl. Phys.* **1951**, 22, 1242.
- [17] A.E. Neeves, M.H. birnboim, *J. Opt. Soc. Am. B* 1989, 6, 787.

- [18] S. Zhu, W. Zhou, *J. Nanomaterials* **2010**, 2010, 1.
- [19] S.K. Ghosh, T. Pal, *Chem. Rev.* **2007**, 107, 4797.
- [20] X.W. Lou, L.A. Archer, Z. Yang, *Adv. Mater.* **2008**, 20, 3987.
- [21] W. Stöber, A.Fink, E. Bohn, *J. Collid. Interf. Sci.* **1968**, 26, 62.
- [22] M.R. Kim, J.-Y. Kim, S.J. Kim, D.-J. Jang, *Appl. Catal. A* **2011**, 393, 317.
- [23] V.R. Calderone, J. Schutz-Widoniak, G.L. Bezemer, G. Bakker, C. Steurs, A.P. Philipse, *Catal. Lett.* **2010**, 137, 132.
- [24] J. Li, C. Yang, L. Zhang, T. Ma, *J. Organomet. Chem.* **2011**, 696, 1845.
- [25] B. Liu, W. Zhang, H. Feng, X. Yang, *Chem. Comm.* **2011**, 47, 11727.
- [26] A.E. Neeves, M.H. Birnboim, *J. Opt. Soc. Am. B* **1989**, 6, 787.
- [27] H.-B. Kim, D.-J. Jang, *Cryst. Eng. Comm.* **2012**, 14, 6946.
- [28] J. Zhu, Y. Wang, L. Huang, Y. Lu, *Phy. Lett. A* **2004**, 323, 455.
- [29] J.J. Penninkhof, A. Moroz, A.V. Blaaderen, *J. Phys. Chem. C* **2008**, 112, 4146.
- [30] A.B. Evlyukhin, A.I. Kuznetsov, S.M. Novikov, J. Beermann, C. Reinhardt, R. Kiyon, S.I. Bozhevolnyi, B.N. Chichkov, *App. Phys. B* **2012**, 106, 841.
- [31] P.K. Jain, K.S. Lee, I.H. El-Sayed, M.A. El-Sayed, *J. Phys. Chem. B* **2006**, 110, 7238.

**Chapter 3. Enhanced Catalytic Performances of Linear-Connected
Platinum Nanobubbles via Laser Welding Process**

3.1. Abstract

Linear-connected platinum nanobubbles have been successfully synthesized without any linkers via the laser welding process. Nanosecond laser have been employed to connect with them and the laser welding process is due to the thermalized photon energy of platinum-plasmon resonances. We have evaluated the catalytic properties of the platinum nanostructures using a reaction based on the reduction of rhodamine B by potassium borohydride and obtained the kinetic parameters (rate constants, activation energies, frequency factors, entropies of activation, and enthalpies of activation) from the first-order kinetics, the Arrhenius plots, and the Eyring plots. The kinetic data indicates that the hollow structures are catalytically more active than core-shell nanostructures and laser-induced platinum nanobubbles have more efficient catalytic performances than that of platinum nanobubbles excluded the laser irradiation step.

3.2. Introduction

Nanostructured materials having functional properties have been extensively investigated to assess the foundations of physical laws at the nanoscales and to pave the way to practical applications [1]. In the particular, noble metal nanostructures have attracted considerable attention scientifically as well as industrially. Noble metal nanostructures have at least one of the following distinctive features: (1) the presence of optically active plasmonic modes which originate intense absorption and scattering bands in the visible-near infrared interval; (2) the easy surface functionalization with a wide series of organic molecules; and (3) the chemical and physical stability and biocompatibility [2-4]. So, noble metal nanostructures can be used in diverse applications in field such as catalysts, devices, transistors, and optoelectronics [5-8]. Properties of noble metal nanostructures are mostly determined by its size, shape, composition, and structures [9,10]. Especially, hollow nanostructures have been studied by many researchers due to their surface plasmonic properties and catalytic activities different from those of solid nanoparticles; in addition, hollow nanostructures have high specific surface area, low density, use less materials, and lower cost [11-13].

A variety of synthetic methods have been demonstrated for preparing noble metal nanostructure. Among them, laser-induced fabrication is the simplest and

the cleanest method. The interaction of the noble metal nanoparticles with pulsed lasers have been the subject of intensive research for more than a decade, with the aim of improving the basic understanding of light-nanomaterial interactions [14-16]. Picosecond and nanosecond laser excitation of the localized surface plasmon resonance (LSPR) band resulted in the melting and size-reduction of noble metal nanoparticles in solution [17]. A model was proposed in which the reshaping form of platinum nanobubbles to a linear-connected platinum nanobubbles have taken place because of the melting of the particle. It is known that the melting points of the platinum nanoparticles are much lower than that of bulk platinum [18]. So, the thermalized photon energy of surface-plasmon excitation induces platinum nanospheres to melt and weld together, producing the linear-connected platinum nanobubbles.

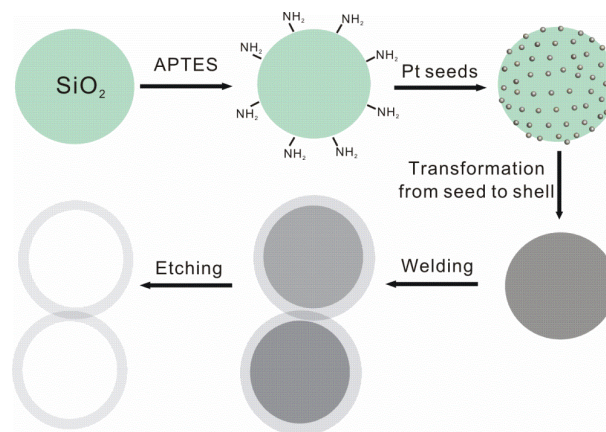


Figure 3-1. Schematic description for the laser-induced fabrication of the connected platinum nanobubbles.

In this work, we have synthesized hollow nanostructures via hard-templating method and connected them using nanosecond laser. Our experiment has four six steps: the preparation of silica hard templates, the functionalization of templates surfaces to achieve favourable surface properties with amino groups, the coating of the templates with platinum seeds, post-treatment to form compact shells, and the selective removal of silica hard templates to obtain hollow structures with hydrofluoric acid [19]. Laser irradiation step has been inserted between post-treatment to form compact shells and the removal of silica hard templates.

3.3. Experimental Section

First, 25.00 mL of ethanol(ℓ), 4.50 mL of deionized water($> 17\text{M}\Omega$), 0.40 mL of 25 % ammonia solution(aq), and 1.55 mL of tetraethyl orthosilicate(ℓ) were mixed and kept under vigorous stirring for 1 h to synthesize the silica hard templates. They were centrifuged with 10,000 rpm for 10 min and redispersed in 31.45 mL of ethanol three times [20,21].

Second, 10.0 mg of $\text{H}_2\text{PtCl}_6(\text{s})$ in 10.00 mL of 35% $\text{HCl}(\text{aq})$, 10.00 mL of 0.2 M $\text{NaBH}_4(\text{aq})$, and 10.00 mL of 0.3 g L^{-1} $\text{PVP}(\text{aq})$ at once, and the solution was not stirred during the reaction to produce the platinum seeds. They were centrifuged at 10,000 rpm for 10 min and redispersed in 30.00 mL of ethanol three times [22].

Third, 10.00 mL of silica hard templates-dispersed in ethanol and 5.00 mL of 1.0 M APTES were mixed and kept under stirring for 2 h to the modification of the surfaces of SiO_2 hard templates with amino groups. Then, 5.00 mL of Pt seeds solution was added and stirred for 1 h to attach the Pt seeds on the silica hard templates.

Fourth, 4.00 mL of 2 days-aged 10 mM $\text{H}_2\text{PtCl}_6(\text{aq})$ and 2.00 mL of the above mixture solution were mixed and stirred for 1 h and 0.32 mL of 100 mM L-ascorbic acid(aq) was added and stirred for 1 h for the transformation of platinum seeds into platinum shells [23].

Fifth, platinum nanobubbles were fabricated by irradiating the above solution with 355 nm nanosecond laser pulse for 1h. The quartz cell was vigorously stirred. The laser irradiation was performed by irradiating the sample with 4 ns pulses of 355 nm having an average 3 mJ from a Quanta Brilliant Q-switched Nd:YAG laser.

Finally, 10.00 mL of aqueous HF and 1.00 mL of above solution were mixed and stirred 2 min [24]. The products were centrifuged at 10,000 rpm for 10 min and redispersed in 1.00 mL of ethanol three times.

Transmission electron microscopic (TEM) images were obtained by microscope (Carl Zeiss, LIBRA 120), and energy-dispersive X-ray (EDX) line-scanning and elemental mapping profiles were measured by using a high resolution microscope (JEOL Ltd., JEM-2100F). Time-dependent extinction spectra of rhodamine B in the presence of potassium borohydride were measured by UV-vis spectrophotometer (Scinco, S-3000). The catalytic performances have been observed by mixing 1.7 mL of 20 μ M rhodamine B, 0.9 mL of H₂O, 0.1 mL of nanocatalyst, and 0.4 mL of 10 mM KBH₄.

3.4. Results and discussion

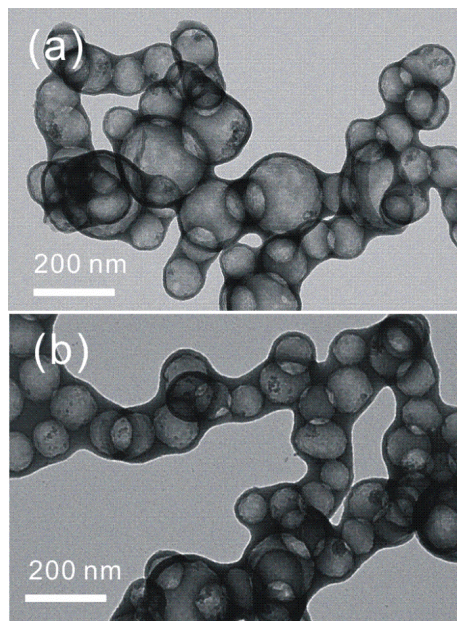


Figure 3-2. Transmission electron microscopy (TEM) images of (a) platinum nanobubbles and (b) laser-induced platinum nanobubbles connected in a line via the laser welding process.

Fig. 2(b) shows that the platinum nanobubbles are connected in a line without any linkers via the laser welding process, whereas Fig. 2(a) shows that the platinum nanobubbles exist separately. The thermalized photon energy of surface-plasmon excitation induces platinum nanospheres to melt and weld together, producing the linear-connected platinum nanobubbles. Because the melting points of the platinum nanoparticles ($600\text{ }^{\circ}\text{C}$) are much lower than that of bulk platinum ($1769\text{ }^{\circ}\text{C}$ at 1 atm pressure), platinum nanoparticles can be

fused by the laser irradiation [18]. Shell thickness has become thick over the laser welding process. This phenomenon can be illustrated by the size reduction of platinum nanobubbles. Exposure to a single-shot laser or a number of shots of pulsed lasers allowed the size reduction. Three types of mechanism have been known to consider size reduction: heating-melting-evaporation concept, photothermal and Coulomb explosion mechanism, and a near-field ablation mechanism [25-31].

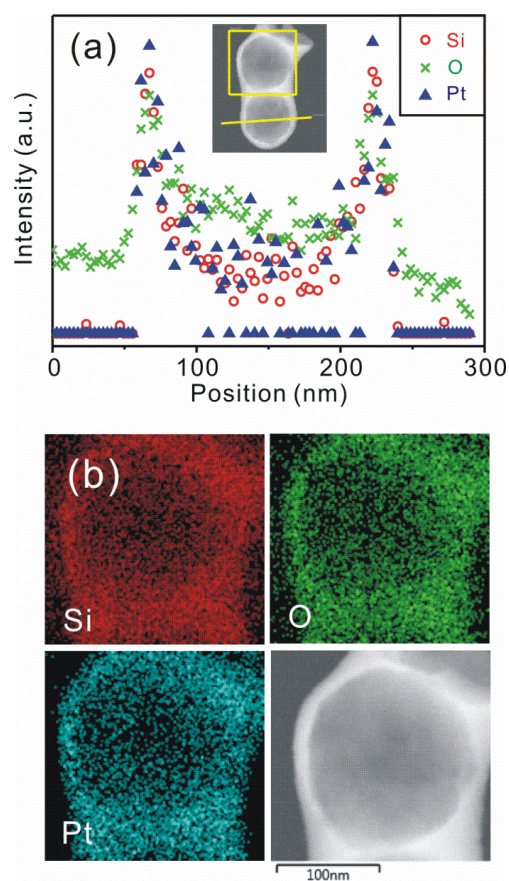


Figure 3-3. (a) EDX elemental line scanning and (b) mapping profiles of laser-induced platinum nanobubbles in the HRTEM image of the inset.

The EDX elemental line scanning profiles in Fig. 3(a) suggests that the platinum nanobubbles have the hollow structure and these nanocatalysts are heterogeneous catalysts because the shapes and positions of two peaks (Si and O) are similar to the respective ones of Pt. Also, the EDX elemental mapping profiles and the electron image of the linear-connected platinum nanobubbles in Fig. 3(b) show that the platinum nanobubbles are well connected each other. Platinum atoms are continuously present without showing discontinuity at the trough in Fig. 3(b) of the platinum mapping profiles, so our programmed laser-induced welding process can be described as the artificial bonding of platinum nanobubbles.

We have studied about the catalytic properties of the platinum nanocatalysts and the effect of the laser welding process on the platinum nanocatalysts. We have monitored the decrease of the rhodamine B maximum peak at 554 nm by mixing the reducing agent of potassium borohydride. Potassium borohydride is nucleophilic and rhodamine B is electrophilic with respect to platinum nanocatalyst, so KBH_4 donates electrons to the platinum nanocatalysts, and rhodamine B obtains electrons from the platinum nanocatalysts. Treatment with the strong reducing agents such as potassium borohydride chemically breaks the double bonds in rhodamine B, producing the lower molecular weight [32,33].

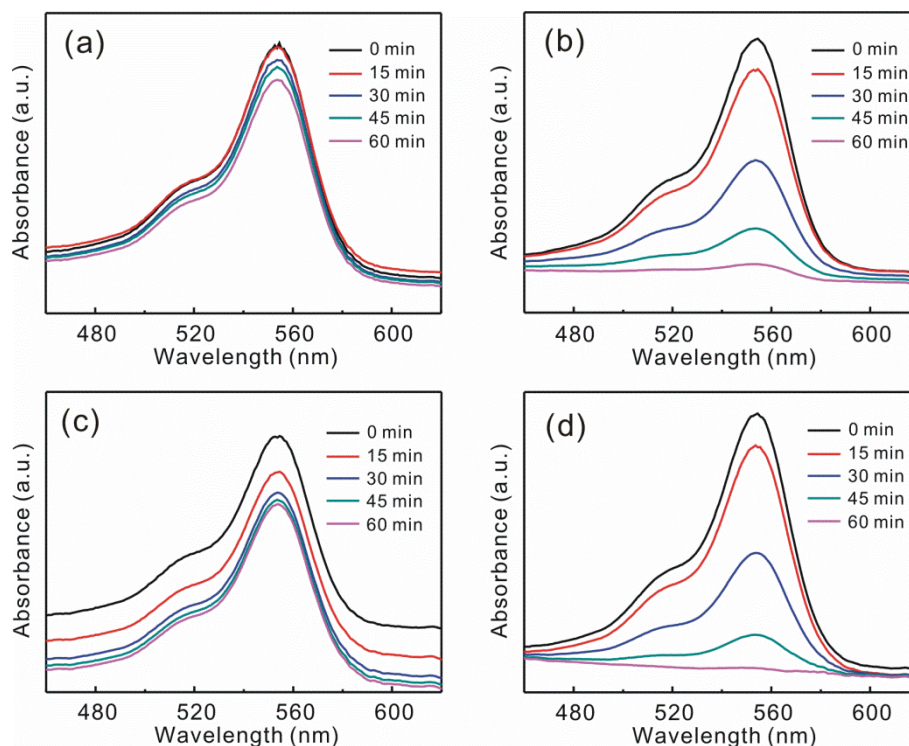


Figure 3-4. Absorption spectra at 30 °C of 11 μM rhodamine B solutions in the presence of 1.3 mM KBH_4 after addition of (a) $\text{SiO}_2\text{@Pt}$ core-shell nanospheres (CNSs), (b) platinum nanobubbles (HNBs), (c) laser-induced $\text{SiO}_2\text{@Pt}$ core-shell nanospheres (L-CNSs), and (d) laser-induced platinum nanobubbles (L-HNBs).

The catalytic properties of platinum nanobubbles with hollow interiors is much more efficient than that of $\text{SiO}_2\text{@Pt}$ core-shell nanostructures, and the nanostructures synthesized by laser-induced fabrication have more efficient performances compared with the nanostructures synthesized by fabrication excluded laser irradiation step. This phenomenon is attributed to the size reduction and increasement of shell thickness. It is known that the melting points of the platinum nanoparticles are much lower than that of the bulk

platinum, so the thermalized energy can fuse the platinum nanoparticles attached on the surfaces, and also helps the platinum precursors in solvent to attach on the surfaces, accelerating the shell connection. These smooth and connected shells are energetically favourable than the spherical platinum nanobubbles.

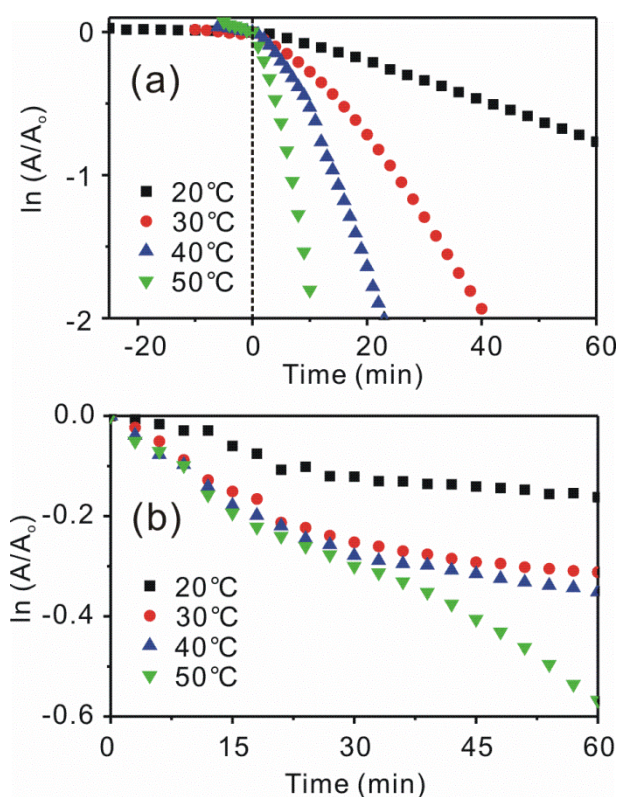


Figure 3-5. The linear relationship between $\ln(A/A_0)$ of rhodamine B corresponding to the rhodamine B degradation by potassium borohydride and the time of the reaction in minutes via the nanocatalysts of (a) L-HNBs and (b) L-CNSs.

Table 3-1. Comparison of the observed rate constants of the catalytic degradation of rhodamine B in the presence of potassium borohydride at different temperatures when catalyzed by L-HNHs and L-CNSs.

Nanocatalyst	20 °C (min ⁻¹)	30 °C (min ⁻¹)	40 °C(min ⁻¹)	50 °C(min ⁻¹)
a	0.0014	0.0047	0.0060	0.0090
L-HNBs	0.012	0.044	0.076	0.17
L-CNSs	0.0032	0.0065	0.0072	0.0094

^a In the absence of any nanocatalysts.

Because the concentration of the BH_4^- ions greatly exceeds those of rhodamine B and the catalysis nanoparticles, pseudo-first-order kinetics [32] with respect to rhodamine B could be used in this case to evaluate the catalytic rate constants; $\ln(A/A_0) = -kt$. We can see that the value of $\ln(A/A_0)$ is constant at the beginning of the reaction and then decrease linearly after a certain time in Fig. 5(a). This period is called as the induction period and it is governed by the diffusion rate of the reacting materials inside the nanocage cavity and the rate the adsorption of the reaction materials on the interior surface of the nanocage in case of the hollow nanocatalyst [35]. The induction period in Fig. 5(a) depends on the temperatures, in a way that it increases with decreasing the temperature and this result agrees well with what was reported earlier by Xia and co-workers [36]. On the other hand when L-CNSs are used as nanocatalyst, the induction period is unobservable. It suggests that the reaction of rhodamine B degradation in the presence of the KBH_4 via L-HNBs takes place within the nanocages and the reaction via L-CNSs nanocatalysts only takes place on the

surfaces of the catalysts.

The degradation rate constant of rhodamine B is obtained by the first-order kinetics from 20 °C to 50 °C at intervals of 10 °C. Using these values, the kinetic parameters (activation energies, frequency factors, entropies of activation, enthalpies of activation) are calculated from the plots shown in Fig. 6. After the reactants reach the surface, the rate of the reaction is determined by the slow-rate determining step of the reaction. The observed rate constant (k_{obs}) is same with the sum of the catalytic degradation rate constants of rhodamine B (k_{cat}) and the degradation rate constant without nanocatalysts (k_0); $k_{\text{obs}} = k_{\text{cat}} + k_0$. Note that the kinetic parameters of nanocatalysts are calculated by k_{cat} .

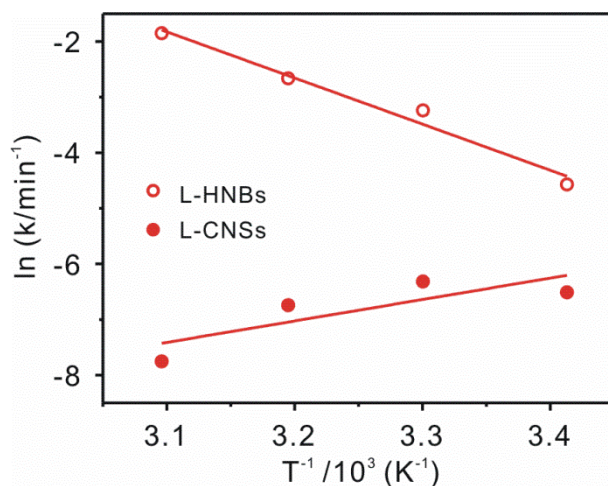


Figure 3-6. The Arrhenius plots for the catalytic degradation reaction of 11 μM rhodamine B solutions in the presence of 1.3 mM KBH_4 via platinum nanocatalysts indicated inside.

Table 2. Summary of the activation energies (E_a), frequency factors (A), the entropies of activation (ΔS), and the enthalpies of activation (ΔH) for the laser-induced platinum nanobubbles and $\text{SiO}_2\text{@Pt}$ core-shell nanospheres

Nanoatalyst	E_a (kcal mol ⁻¹)	A (min ⁻¹)	ΔS (kcal mol ⁻¹ K ⁻¹)	ΔH (kcal mol ⁻¹)
L-HNBs	0.0057	2.4×10^{10}	-13.10	6.31
L-CNSs	-7.63	3.88×10^{-9}	-99.08	-3.29

We have obtained the catalytic activation energies and frequency factors from the slope and y-intercepts of the Arrhenius plots [36] in Fig. 6. The entropies and enthalpies of activation have been obtained by the Eyring plots [37]; $\ln(k_f/T) = -\Delta H/(RT) + \Delta S/R + \ln(k_b/h)$. Reaction via L-HNBs has very small activation energy compared with non-connected platinum nanobubbles. The frequency factor of L-HNBs ($2.4 \times 10^{10} \text{ min}^{-1}$) in Table 2 is much higher than reported frequency factor of non-connected platinum nanobubbles ($1.6 \times 10^6 \text{ min}^{-1}$) and it is consequentially connected with the fact that the activation energy of L-HNBs is much small than that of non-connected platinum nanobubbles [38]. But, the reaction via L-CNSs is characterized by having so-called negative activation energy, i.e., the rate decreases with increasing temperature. The occurrence of negative activation energies is due to the formation of an intermediate complex [39,40]. The behaviour of reactions having a negative temperature dependence has been successfully described by Mozurkewich and Benson [41]. Large negative temperature dependences are found in very fast solution reactions.

3.5. Conclusions

We have successfully synthesized linear-connected platinum nanobubbles without any linkers via the laser welding process and we have obtained the kinetic parameters of degradation of rhodamine B via synthesized platinum nanocatalysts to investigate the laser irradiation effect. After the laser irradiation, the edge of nanocatalysts have been melt and welded. Also, sizes of nanocatalysts have been decreased and shell thickness has become thick. This is due to the thermalized photon energy of platinum-plasmon resonances and it makes the linear-connected platinum nanobubbles have more efficient catalytic performances.

3.6. References

- [1] J.-Y. Kim, H. Jeong, D.-J. Jang, *J. Nanopart. Res.* **2011**, 13, 6699.
- [2] Y. Xia, N.J. Halas, *MRS Bull.* **2005**, 30, 338.
- [3] M.C. Daniel, D. Astruc, *Chem. Rev.* **2004**, 104, 293.
- [4] C.J. Murphy, A.M. Gole, J.W. Stone, P.N. Sisco, A.M. Alkilany, E.C. Goldsmith, S.C. Baxter, *Acc. Chem. Res.* **2008**, 41, 1721.
- [5] E.C. Dreaden, M.A. El-Sayed, *Acc. Chem. Res.* **2012**, 45, 1854.
- [6] A. Takami, H. Kurita, S. Koda, *J. Phys. Chem. B* **1999**, 03, 1226.
- [7] Y.-J. Han, J.M. Kim, G.D. Stucky, *Chem. Mater.* **2000**, 12, 2069.
- [8] R. Cartrin, D. Horwat, J.-F. Pierson, S. Migot, Y. Hu, F. Mücklich, *Appl. Surf. Sci.* **2011**, 257, 5223.
- [9] J. Gao, X. Ren, D. Chen, F. Tang, J. Ren, *Scripta Materialia* 2007, 57, 687.
- [10] R. Jin, Y. Cao, C.A. Mirkin, K.L. Kelly, G.C. Schatz, J.G. Zheng, *Science* **2001**, 294, 1901.
- [11] S.W. Kim, M. Kim, W.Y. Lee, T. Hyeon, *J. Am. Chem. Soc.* **2002**, 124, 7642.
- [12] Y. Sun, Y. Zia, *Anal. Chem.* **2002**, 4, 5297.
- [13] H.P. Liang, H.M. Zhang, J.S. Hu, Y.G. Guo, L.J. Wan, C.L. Bai, *Angew. Chem. Int. Ed.* **2004**, 43, 1540.
- [14] G.V. Hartland, *Chem. Rev.* 2011, 111, 3858.

- [15] C. Burda, X. Chen, R. Narayanan, M.A. El-Sayed, *Chem. Rev.* **2005**, 104, 1102.
- [16] S. Link, M.A. El-Sayed, *Int. Rev. Phys. Chem.* **2000**, 19, 409.
- [17] D. Werner, S. Hashimoto, *Langmuir* **2013**, 29, 1295.
- [18] Z.L. Wang, J.M. Petroski, T.C. Green, M.A. El-Sayed, *J. Phys. Chem. B.* **1998**, 102, 6145.
- [19] X. Wen, L.A. Archer, Z. Yang, *Adv. Mater.* **2008**, 20, 3987.
- [20] W. Stöber, A.Fink, E. Bohn, *J. Collid. Interf. Sci.* **1968**, 26, 62.
- [21] M.R. Kim, J.-Y. Kim, S.J. Kim, D.-J. Jang, *Appl. Catal. A* **2011**, 393, 317.
- [22] V.R. Calderone, J. Schutz-Widoniak, G.L. Bezemer, G. Bakker, C. Steurs, A.P. Philipse, *Catal. Lett.* **2010**, 137, 132.
- [23] J. Li, C. Yang, L. Zhang, T. Ma, *J. Organomet. Chem.* **2011**, 696, 1845.
- [24] B. Liu, W. Zhang, H. Feng, X. Yang, *Chem. Comm.* **2011**, 47, 11727.
- [25] S. Hashimoto, D. Werner, T. Uwada, *J. Photochem. Photobio. C*
- [26] S. Link, M.B. Burda, B. Mohamed, B. Nikoobakht, M.A. El-Sayed, *J. Phys. Chem. A* **1999**, 103, 1165.
- [27] S. Link, M.B. Burda, B. Nikoobakht, M.A. El-Sayed, *J. Phys. Chem. B* **2000**, 104, 6152.
- [28] F. Giammanco, E. Giorgetti, P. Marsili, A. Giusti, *J. Phys. Chem. C* **2010**, 114, 3354.
- [29] A. Plech, V. Kotaidis, M. Lorenc, J. Bonberg, *Nat. Phys.* **2006**, 2, 44.

- [29] D. Werner, A. Furube, T. Okamoto, S. Hashimoto, *J. Phys. Chem. C* **2011**, 115, 8503.
- [30] G.W. Wang, *Prog. Mater. Sci.* **2007**, 52, 648.
- [31] N.G. Semaltianos, *Crit. Rev. Solid State Mater. Sci.* **2010**, 35, 105.
- [32] Z. Deng, M. Chen, L. Wu, *J. Phys. Chem. C* **2007**, 111, 11692.
- [33] Z.J. Jiang, C.Y. Liu, L.W. Sun, *J. Phys. Chem. B* **2005**, 109.
- [34] N.S. Langeroodi, *Rus. J. Phys. Chem. A* **2012**, 86, 628.
- [35] M.A. Mahumaud, M.A. El-Sayed, *Nano Lett.* **2011**, 11, 946.
- [36] J. Zeng, Q. Zhang, J.Y. Chen, Y.N. Xia, *Nano Lett.* **2010**, 10, 30.
- [37] K.D. Zimmer, R. Shoemaker, R.R. Ruminski, *Inorg. Chim. Acta* **2006**, 359, 1478.
- [38] J.-A. Kwak, D. Lee, D.-J. Jang, *Appl. Catal. B: Environ.* **2013**, 142, 323.
- [39] J.A.-I Raül, M.-D. Nelaine, V.-B. Annik, *J. Am. Chem. Soc.* **2000**, 122, 3715.
- [40] T. Shimomura, K.J. Tölle, J. Smid, M. Szwarc, *J. Am. Chem. Soc.* 1967, 89, 796.
- [41] M. Mozurkewich, S.W. Benson, *J. Phys. Chem.* **1984**, 88, 6429.

Appendices

A.1. List of Publications

1. **Jin-Ah Kwak**, Dong Ki Lee, Du-Jeon Jang, “Facile fabrication of platinum nanobubbles having efficient catalytic degradation performances”, *Appl. Catal. B: Environ.* **2013**, 142-143, 323-328.

A.2. List of Presentations

A.2.1. International Presentation

1. **Jin-Ah Kwak** and Du-Jeon Jang, “Enhanced Catalytic Properties of Platinum Nanoshell Structures”, *The first Photocatalysis and Solar Energy Convention: Development of Materials and Nanomaterials*, Deajeon, Korea (2012).

A.2.2. Domestic Presentation

1. **Jin-Ah Kwak** and Du-Jeon Jang, “Fabrication of Platinum Nanobubbles Having Enhanced Catalytic Properties”, *The 109th Spring Meeting of the Korean Chemical Society*, Goyang, Korea (2012).
2. **Jin-Ah Kwak, Dong Ki Lee**, and Du-Jeon Jang, “Catalytic Properties of Pt Nanoshells Synthesized via Acid Etching of SiO₂@Pt Nanospheres”, *The 110th Autumn Meeting of the Korean Chemical Society*, Busan, Korea (2012).

Abstract (Korean)

백금 기반 나노 구조체의 촉매적 활성을 시간 의존적 자외선/가시광선 영역 흡수 분광학을 이용하여 연구를 하였으며, Mie 이론에 의거한 백금의 표면 플라즈몬 공명을 계산하였다.

1 장에서는 백금 기반의 향상된 촉매 활성을 가지는 속빈 나노 셀 구조체를 크기 별로 합성하고, 속빈 구조를 고해상도 전자현미경을 통해 확인하였다. 속빈 나노 셀 구조체는 속이 찬 구형의 구조에 비해 표면적 증가 및 구속효과를 가지게 되어 환원제를 이용한 유기 염료 분해를 촉진시키며, 이는 시간 의존적 자외선/가시광선 영역대 흡수 분광학을 통해 관찰되었다. 유기 염료 분해 실험 시 얻어진 활성화 에너지를 통해 현상을 수치적으로 설명할 수 있었으며, 여러 가지 동역학적 계수들을 통해 일반적인 촉매 시스템에서 발견되는 보상효과가 백금 기반의 속빈 나노 셀 구조체에도 적용되었음을 기술하였다.

2 장에서는 반지름 74 nm, 11 nm의 셀 두께를 가지는 $\text{SiO}_2@Pt$ 코어-셀 나노구와 속빈 백금 나노버블의 표면 플라즈몬 공명에 대해 기술하였다. Mie 이론을 통한 표면 플라즈몬 밴드 계산 값과 세 가지 용매에 분산된 정류상태 자외선/가시광선 영역대 흡수 분광 스펙트럼을 비교함으로써 기존에 이루에 지지 않았던 백금의 표면 플라즈몬 현상에 대한 기술을 시도하였다.

3 장에서는 귀금속 나노 구조물의 광유도 나노 접합에 대하여 논하고 있다. 1 장에서 합성된 백금 기반의 속빈 나노 셀 구조체에 나노초 레이저 펄스를 조사하면 인접된 입자의 가장자리 부분이 접합된다. 이는 고해상도 투과전자 현미경과 에너지 분산형 엑스선 분광기를 통해 확인되었으며, 표면 플라즈몬 여기에 의한 열중성자화된 광자 에너지로 인한 현상으로 설명할 수 있다. 또한, 셀 접합에 의한 효과가 촉매 특성에 미치는 영향을 동력학적 계수로 수치화하여 설명하였다.

주요어: 백금, 나노버블, 코어-셀 나노구, 촉매반응, 표면 플라즈몬 공명, Mie 이론, 레이저 접합

학번: 2011-2314